
Beamline for Materials Measurement (BMM)

Beamline Final Design Report

CONTENTS

	Acronyms	2
	Abstract	4
	Introduction	4
	Axes Definition	5
1	Scientific Programs and Technical Scope	6
1.1	Local Structure and Phase Transitions in Electronic Ceramics	7
1.2	Local Structure Function Properties of Strain Engineered Electronic Thin Films	8
1.3	Understanding Radiation Damage in Nuclear Materials with Glancing Angle XAFS	9
1.4	In situ Characterization of Commercial Catalysts: From Understanding to Development	10
1.3	Technical Scope	12
1.4	End-station	14
1.5	Development and Advisory Team	14
2	BMM beamline	16
2.1	Source	16
2.2	Front End	17
2.3	Vertical and Horizontal Collimating Mirror	20
2.4	First Optical Enclosure	24
2.5	Beamline Optics	27
2.6	Monochromator	32
2.7	M2: Toroidal focusing mirror	35
2.8	M3: Planar harmonic rejection mirror	38
2.9	Radiation Shielding	41
3	End station	45
3.1	End station diagnostics	46
3.2	XAFS End station	48

3.3	Diffraction End station	49
3.4	Beamline Utilities.....	50
3.5	Equipment Protection System.....	54
3.6	Personnel Protection System.....	55
3.7	Laboratory Space and Access	56
3.8	Work Area	57
4	Major Technical Risk Items	59
4.1	Beamline complexity driven by mirror system operating modes	59
4.2	Relocation and re-use of end station equipment, poorly specified end station equipment	59
4.3	Monochromator heat load	59
4.4	Presence of M1 in the front end.....	60
4.5	Platinum substrate on mirrors M1 and M2	60
5	Safety	61
	Appendices	63

Acronyms

BDP	Beamline Development Proposal
BMM	Beamline for Materials Measurement
DCM	Double-Crystal Monochromator
EPS	Equipment Protection System
EXAFS	Extended X-ray Absorption Fine Structure
FE	Front End
FM	Fixed Mask
FOE	First Optical Enclosure
HRM	Harmonic Rejection Mirror
ISS	Inner Shell Spectroscopy beamline
NEXAFS	Near Edge X-ray Absorption Fine Structure
PPS	Personnel Protection System
SST	Beamline for Spectroscopy, Soft and Tender
TFM	Toroidal Focusing Mirror
TPW	Three Pole Wiggler

VHC	Vertical and Horizontal Collimating Mirror
XAFS	X-ray Absorption Fine Structure spectroscopy
XANES	X-ray Absorption Near Edge Structure
XRD	X-ray Diffraction
XBPM	X-ray Beam Position Monitor

Abstract

The Beamline for Materials Measurement (BMM) beamline is one of the suite (SST1&2, and BMM) of state-of-the-art, high-throughput, spectroscopy beamlines at the NSLS-II developed by the National Institute of Standards and Technology (NIST) and located at port 6BM. The scientific case and capability of BMM was introduced in the beamline development proposal (BDP): *NIST Spectroscopy Beamline Suite: Hard X-ray Absorption Spectroscopy and Diffraction*. This final design report (FDR) covers

- a brief summary of the scientific case,
- the design of the beamline in terms of the front-end, First Optical Enclosure (FOE), and transport pipe design, along with analysis of radiation shielding design including that of Bremsstrahlung, secondary Bremsstrahlung and synchrotron x-rays of the source (three pole wiggler) and design of the optics (collimating mirror in front-end, monochromator using Silicon 311 and 111 reflections, followed by either a focusing or a flat mirror or both),
- a discussion of end station equipment for XAFS and diffraction, including items that will be transferred from the NSLS to the BMM beamline, and
- a summary of technical risks and safety considerations.

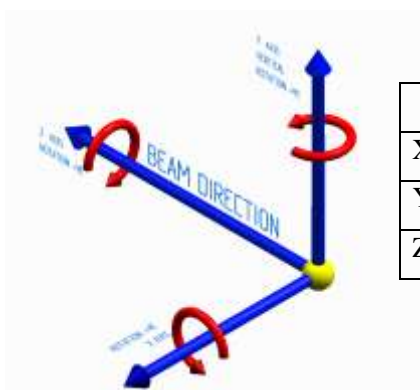
Introduction

The National Institute of Standards and Technology (NIST) and the Department of Energy (DOE) have a partnership at the National Synchrotron Light Source that spans over three decades and continuing into operations at NSLS-II. In that time, NIST has developed advanced synchrotron measurement methods and delivered excellence in material science, impacting important societal challenges in energy, health, environment, national security, and improving our quality of life. This partnership promotes innovation and enhances US industrial competitiveness in areas such as inorganic and organic semiconductors, photovoltaics, self-assembled monolayers (SAMs), biological and environmental materials, batteries, catalysts, fuel cells, polymers, superconductors, ferroelectrics, and ferromagnets. At the NSLS, the NIST Synchrotron Methods Group operated a suite of three state-of-the-art spectroscopy beamlines (U7A, X24A, and X23A2) that spanned the absorption-edge energy range of the entire periodic table to establish structure function relationships in advanced materials. More than 200 industry and academic researchers each year used the NIST NSLS Beamline Suite to accelerate the development of new materials into devices and systems with advanced functionality for a broad spectrum of industries. Building upon this success, NIST is currently developing an NSLS-II spectroscopy suite of three state-of-the-art high throughput beamlines with X-ray Diffraction capability described in two beamline development proposals for the NIST Spectroscopy Beamline Suite: *Soft and Tender X-ray Spectroscopy and Microscopy* and *Hard X-ray Absorption Spectroscopy and Diffraction*. Taken together, the NIST Spectroscopy Beamline Suite at NSLS-II will be capable of measuring electronic, chemical, and structural properties of almost any material, often at the nanoscale. NIST is committed to fully funding the construction of its proposed Spectroscopy Beamline Suite and to continuous world leading improvements in synchrotron measurement science and technology. Furthermore, NIST will build

upon its BNL-based Synchrotron Methods Group to fully staff its stakeholder relationship in NSLS-II.

Axes Definition

Unless otherwise specified, the axes definition used in this document is shown in Figure 1. X-rays travel in the positive Z direction and X is the horizontal direction where positive is away from the storage ring. The vertical axis is Y, where up is positive. Rotations are referred according to the rotation axis.



	Directions	Rotations
X	Outboard is positive	ΘX is rotation about X-axis
Y	Up is positive	ΘY is rotation about Y-axis
Z	X-ray direction is positive	ΘZ is rotation about Z-axis

NSLS-II convention for axes definition used in this PDR.

1 SCIENTIFIC PROGRAMS AND TECHNICAL SCOPE

In this document, we outline NIST's plans to develop a spectroscopy and scattering beamline at NSLS-II port 6BM using a three-pole wiggler (TPW) source. BMM is a facility primarily for efficient, high-throughput X-ray Absorption Spectroscopy (XAS) and has been designed to take advantage of the beam characteristics of the NSLS-II TPW source for high resolution XAS measurements. The beamline will also add new X-ray diffraction (XRD) capabilities to complement NIST's existing XAS program and to supplement the materials measurement mission of the beamline. The X-ray optics are designed to provide either focused or collimated X-rays at the sample, for both high resolution XAS and diffraction experiments. The X-ray diffraction end station can take advantage of the scanning capabilities of the beamline, adding glancing incidence XAS and XAS at constant q (i.e. reflectivity XAS and diffraction anomalous fine structure (DAFS)) to NIST's many other spectroscopic tools for materials science study. Polarization dependent XAFS measurements will also benefit from the high-precision six-circle goniometer and its ability to accurately and quickly position samples relative to the X-ray beam. Together, this instrumentation along with a variety of *in situ* sample environments will serve a broad range of structural characterization problems in materials science.

The XAS and XRD capabilities of the BMM beamline coupled with NIST's continuous development of automated, high-throughput spectroscopy methods and high-quality, high efficiency detectors will combine to have a large scale impact on the materials science of important societal challenges in energy, health, environment, and national security.

In sections 1.1 to 1.4, we highlight some areas of scientific interest for the BMM beamline with four examples:

1. Local Structure and Phase Transitions in Electronic Ceramics, *I. Levin (NIST)*
2. Local Structure Function Properties of Strain Engineered Electronic Thin Films, *J.C. Woicik (NIST)*
3. Understanding Radiation Damage in Nuclear Materials with GA-XAS, *N. Hyatt, D. Reid, M. Stennet (U. Sheffield), B. Ravel(NIST)*
4. *In situ* Characterization of Commercial Catalysts: From Understanding to Development, *S.R. Bare (UOP)*

These cases illustrate how BMM will establish structure-function relationships in advanced materials, often at the nanoscale, to accelerate the development of new materials into devices and systems with advanced functionality for promoting innovation and enhancing US industrial competitiveness.

1.1 Local Structure and Phase Transitions in Electronic Ceramics

Exploitable properties of advanced electronic ceramics are intimately connected to fine details of atomic arrangements. Practical device applications require simultaneous optimization of several functional characteristics of these materials which is addressed via modifications of their crystal structures using complex chemistry. As a result, local atomic arrangements frequently deviate from those described by the average crystal structure. In many cases, such local deviations control the functional properties. Therefore, establishing comprehensive structure-property relations requires accurate knowledge of local structure details and understanding of the interplay between the local and average atomic arrangements. XAFS and diffraction are the main measurement tools for addressing this problem.

The BMM beamline will combine high-resolution X-ray diffraction with X-ray absorption spectroscopy in the same experiment. These measurements will permit simultaneous determination of the average structure and chemically-resolved local coordination using the same sample under identical environmental (temperature, atmosphere) conditions. Such combined measurements will enable variable-temperature/controlled-atmosphere studies of structural changes by eliminating usual ambiguities associated with somewhat different sample environments in different experimental set-ups. Combining the two experiments will significantly decrease (by about a factor of two!) the overhead time associated with heating/cooling and equilibrating the sample at each temperature. This overhead becomes more significant as more temperatures are included in an experiment.

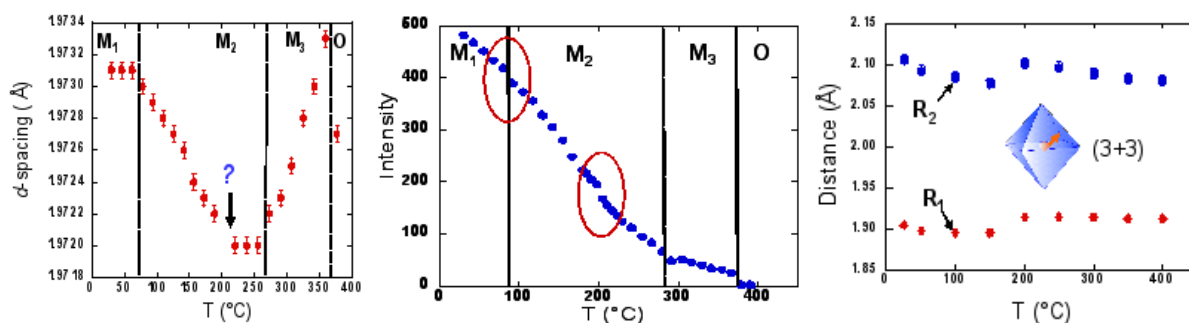


Figure 1.1: (Left) Temperature dependence of (left) 220 d-spacing in AgNbO_3 and (center) intensity of the superlattice reflection associated with ordering of Nb displacements. Phase transitions are indicated as well as some additional anomalies. (Right) Temperature dependence of Nb-O distances extracted from Nb EXAFS. Local displacements of Nb are indicated. Note the anomaly around 200 °C which seemingly correlates with anomalies seen in diffraction (Fig. 1). Accurate knowledge of absolute temperatures in both experiments is necessary to ascertain these correlations.

One typical example of work that illustrates the potential benefits of the new facility is our recent study of local displacive order and its effect on the diffuse phase transition in $\text{Ag}(\text{Nb,Ta})\text{O}_3$ dielectrics¹. $\text{Ag}(\text{Nb,Ta})\text{O}_3$ is the only known system that exhibits large temperature stable dielectric constants combined with modest dielectric losses at microwave frequencies. These remarkable properties have been attributed to a high-frequency dielectric relaxation which yields a broad peak in the temperature dependence of dielectric constant. Our studies using a combination of several diffraction and spectroscopic techniques concluded that this transition reflects long-range ordering of local Nb displacements into an anti-polar array within the symmetry defined by the tilted $[\text{NbO}_6]$ octahedral framework. A combination of average anti-polar Nb displacements and residual displacive Nb disorder explains a broad peak of dielectric constant and the underlying dielectric relaxation. The conclusions of our work suggested ways of synthesizing other systems with similar properties.

1.2 Local Structure Function Properties of Strain Engineered Electronic Thin Films

Strain engineering via epitaxial thin-film growth is an effective method by which the electronic and mechanical properties of a material may be custom tailored. Industrial applications range from enhanced electron mobility devices² to the recently demonstrated realization of ferroelectric memory conjoined with silicon^{3,4}. Strain also alters both the nature and temperature of ferromagnetic, ferroelectric, and superconducting phase transitions.⁵

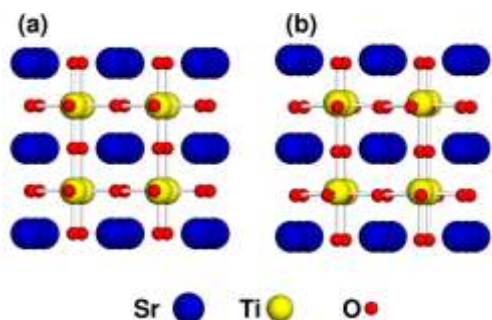


Figure 1.2: (a) Structure of cubic SrTiO_3 . (b) Structure of strained SrTiO_3 on $\text{Si}(001)$ as calculated by DFT. The structure in (b) reveals both AFD and FE distortions.³

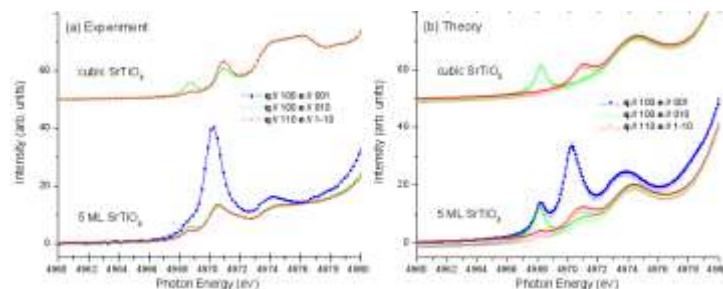


Figure 1.3: (a) Ti K near-edge spectra for cubic SrTiO_3 and a monolayer (2 nm) SrTiO_3 thin film grown coherently on $\text{Si}(001)$. (b) Theoretical spectra calculated³ from the structures from Fig. 3.

With the BMM beamline, users will have the ability to combine high-resolution, polarization-dependent, near and extended XAFS measurements with XRD to determine the strain and local structural distortions in strained, epitaxial thin films grown on substrates with dissimilar lattice constants. These measurements will have the goal of improving both first principles and phenomenological theoretical modeling of the unique structures and rich phase diagrams that

1. [I. Levin, et al, *Phys. Rev. B.*, **79**:10, 104113 \(2009\)](#)
2. [M.L. Lee, et al., *J. Appl. Phys.* **97**, 011101 \(2009\).](#)
3. [J.C. Woicik, et al, *Phys. Rev. B* **75**, *Rapid Communications*, 140103 \(2007\).](#)
4. [M.P. Warusawithana, et al., *Science* **324**, 367 \(2009\).](#)
5. [D.G. Schlom, et al., *Annu. Rev. Mater. Res.* **37**, 589 \(2007\)](#) and references therein.

these materials reveal.

As an example of our previous work, Figure 1.3 shows the polarization-dependent near edge XAFS spectra from a thin, 5 monolayer (2 nm) SrTiO₃ film grown coherently on Si(001) by Motorola⁸. The enhancement of the pre-edge peak is direct evidence for the presence of a room-temperature ferroelectric polarization in the film normal to the film/substrate interface, and it is reproduced by *ab initio* density functional theory calculations of both the atomic and electronic structure of strained SrTiO₃ (Figure 1.3). SrTiO₃ is normally not ferroelectric at any temperature, so the strain imposed on the film by the substrate has created a “new” and directly observable phase of SrTiO₃. As a direct result of this research, initial steps towards the industrially relevant goal of high-density, nano-sized, non-volatile ferroelectric memory written and read on a 2 nm SrTiO₃ thin film on Si were made.

The spectra shown in Figure 1.3 were collected at the NIST beamline X23A2 in a glancing-incidence, thin-film geometry to limit the X-ray penetration into the Si substrate. As X23A2 had no focusing optics, each spectrum required 2 to 3 days (6 to 9 eight hour shifts) of beam time to obtain high quality EXAFS data. Thin-film research will therefore greatly benefit from the new NIST BMM.

1.3 Understanding Radiation Damage in Nuclear Materials with Glancing Angle XAFS

A legacy of the civil and military fuel cycles in the UK and elsewhere is a stockpile of separated plutonium which constitutes a considerable proliferation and security risk. Ultimately, a fraction of this stockpile will require immobilization in a durable and passively safe matrix, suitable for final disposal. A key element of the disposal system safety case is reliable prediction of the evolution of the immobilization matrix under the influence of radiation damage arising from actinide α -decay, which eventually results in a crystalline to amorphous phase transition. Our study⁶ using Grazing Angle XAFS (GA-XAFS) on beamline X23A2 was the first to quantify the effect of radiation damage on the co-ordination environment of key elements in model immobilization systems such as zirconolite – CaZrTi₂O₇.

To simulate radiation damage caused by α -recoil in model immobilization ceramics, we use 2 MeV Kr⁺ implantation which results in a fully amorphized surface layer about 1 μ m in thickness. Consideration of X-ray penetration depth shows that even at the Ti K edge, XAS data acquired in conventional 45° fluorescence mode are dominated by sampling of the undamaged interior of the specimen. By careful selection of the incident grazing angle, XAS data are acquired only from the radiation-damaged surface layer. Ti K-edge XANES are especially sensitive to the local symmetry of Ti, Fig. 1.4. Analysis of the height and position of this feature confirms a transformation to ~100% 5-fold coordination in the damaged surface layer, compared to the crystalline pristine material which contains both 6- and 5-fold co-ordinate Ti in the ratio 2:1, Fig 8.

1. ⁶ [D.P. Reid, et al, Nuclear Instruments and Methods in Physics Research, B268 \(2010\) 1847](#)

Quantitative analysis of EXAFS data measured in this geometry confirmed the XANES analysis. Following sample irradiation, EXAFS data show a loss of fine structure consistent with the loss of long range periodicity, Fig. 1.5. The FT $\chi(k)$ show a near complete suppression of signal beyond the first shell, consistent with the loss of long range periodicity. GA-XAS spectra acquired from 2 MeV Kr^+ irradiated zirconolite were found to be indistinguishable from that acquired from a fully radiation amorphized (i.e. metamict) zirconolite mineral (dated to > 500 Ma).

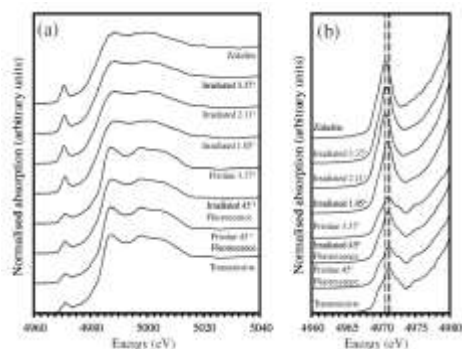


Figure 1.4: a) Ti K edge XANES spectra of zirconolite acquired in transmission and fluorescence mode (at varying angles of incidence); (b) detail of pre-edge XANES feature.

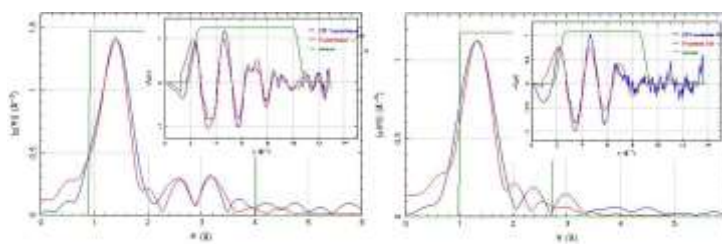


Figure 1.5: FT $\chi(k)$ and $k^2\chi(k)$ data (inset) for pristine (top) and 2 MeV Kr^+ amorphized (bottom) $\text{CaZrTi}_2\text{O}_7$; data in blue and fit in red; data collected in transmission and grazing angle mode, respectively.

In coming years, we will apply this methodology to investigate the radiation amorphized structure of a variety of potential host matrices with the aim of establishing systematic damage-structure-property relations. Crucially, this will enable the study of radiation damaged materials for which no natural mineral analogues exist. Future development of this methodology will benefit significantly from the capabilities of BMM, including higher flux, excellent energy resolution due to the use of Si(311) crystals, and the availability of an eight-circle goniometer.

1.4 In situ Characterization of Commercial Catalysts: From Understanding to Development

UOP LLC, headquartered in Des Plaines, IL, USA, is a leading international supplier and licensor of process technology, catalysts, adsorbents, process plants, and consulting services to the petroleum refining, petrochemical, and gas processing industries. UOP is a wholly-owned subsidiary of Honeywell International, Inc. and is part of Honeywell's Specialty Materials strategic business group. UOP has been using synchrotron radiation primarily to probe the structure of its catalysts and adsorbents since the early 1980's and was a charter member of the original Matrix PRT at the NSLS in the mid-1980's. UOP has collaborated with NIST at the NSLS for many years.

The successful commercialization of a catalyst involves many different steps from the initial discovery, to scale-up and manufacturing, and finally to commercial service. The use of X-ray

absorption spectroscopy (XAS) to provide local chemical and structural information of a particular element in a catalyst is a technique of choice at UOP for all steps in this process. The well-known strengths of XAS are fully utilized, particularly the *in situ* methodology. The capabilities of BMM will fully meet the needs of such a catalyst development program.



Figure 1.6: Representation of the Sn-beta zeolite structure as derived from the EXAFS data, viewed along the b-axis (for clarity the oxygen atoms are not shown). The only Sn distribution consistent with the EXAFS data is one where pairs of Sn atoms occupy opposite vertices of the six-member rings.

One goal of catalysis science is to develop catalysts that are 100% selective to the desired product. The substitution of a heteroatom into a zeolite provides new functionality of the material leading to new applications, often providing isolated active sites that are indeed 100% selective⁷. In such a catalyst, there are fundamental questions for which EXAFS is an ideal tool: (1) does the heteroatom substitute into the framework? (2) does it exist as an extra-framework species? (3) what is the crystallographic location of the atom? EXAFS was successfully used to show that the substitution of Sn into the β -zeolite structure leads to the formation of a unique paired Sn site (Fig. 1.6) that is believed to give rise to the unique 100% selectivity of this catalyst for many oxidation reactions⁸. We envision using *in situ* XAS to probe the structure of many similar heteroatom-substituted zeolites at BMM. Here, however, advantage will be made of using both the XRD and XAS, so both the local and long range structure can be probed.

This is particularly important in zeolitic materials where it is known that the zeolitic structure can be damaged due to processing conditions such as steaming or high temperature operation.

After a catalyst is developed and progresses from laboratory-scale (tens of grams of material) to scale-up where kilogram quantities are produced to manufacturing where the unit is now tons - then the emphasis shifts from fundamental understanding to rapid commercialization, where throughput (productivity) and turnaround time (direct relevance) are key drivers. At this stage often subtle changes in formulation or preparation conditions results in a change of catalyst performance. The ability to detect any structural changes is critical to having an impact on a catalyst development program, where a correlation can be made to conversion and selectivity. The recent combined development between NIST, UOP, and BNL of a four-channel ionization chamber for XAS measurements, combined with the appropriate *in situ* reactor have revealed that such subtle structural changes can be measured in fully-formulated commercial catalysts⁹. Such methodology will be used at BMM along with the increased flux, the advanced control and data management/processing, and the excellent energy resolution of the Si(311) monochromator.

7 [Corma, A.; Nemeth, L.T.; Renz, M.; Valencia, S. *Nature* **2001**, 412, 423-425.](#)

8 [S.R. Bare, et al., *J. Am. Chem. Soc.* **127** \(2005\) 12924-12932.](#)

9 [S.R. Bare, et al., *Physical Chemistry Chemical Physics*, 2010](#)

1.3 Technical Scope

BMM beamline is a facility primarily for efficient, high-throughput X-ray Absorption Spectroscopy (XAS) with an additional mission of high-quality X-ray Diffraction (XRD) for materials measurement. The BMM uses a three-pole wiggler source and is designed to operate in the range from 4.5 keV to 23 keV using Si(111) and Si(311) monochromator crystals. The optical design was developed in collaboration with Reuben Reininger. Fig 1.7 shows a schematic layout of the BMM optics. After the vertically and horizontally collimating (VHC) mirror at 13 m in the front end, there is a pink beam diagnostic module, followed by a DCM which was built by FMB-Oxford in 2010 and is already present at BNL. A monochromatic beam diagnostic module is located downstream of the DCM. These are followed by the following optics: a cylindrical focusing mirror that may be bent to a toroid (M2-TFM) to provide either horizontally or horizontally and vertically focused beam and a flat mirror that may be used to either reject harmonics or to deliver the collimated X-rays from the VHC when required for non-specular x ray diffraction (M3-HRM). Following these optics are a monochromatic beam shutter and diagnostics, including a nanoBPM (see Section 3.1). These components are connected by transport pipe, vacuum equipment, stands, and bellows. Beam transport outside of the optics hutch will be lead-wrapped.

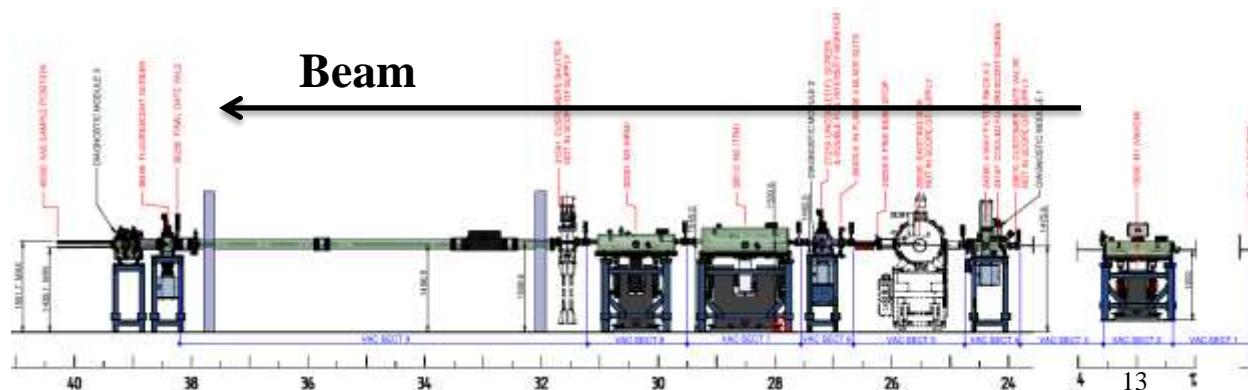


Fig 1.7: Schematic layout of the BMM optics. Beam direction is from right to left. Note that the VHC is placed inside the shield wall to maximize both vertical and horizontal aperture that can be collected. The DCM, TFM, and other components are in the FOE. Note scale break at 14 meters.

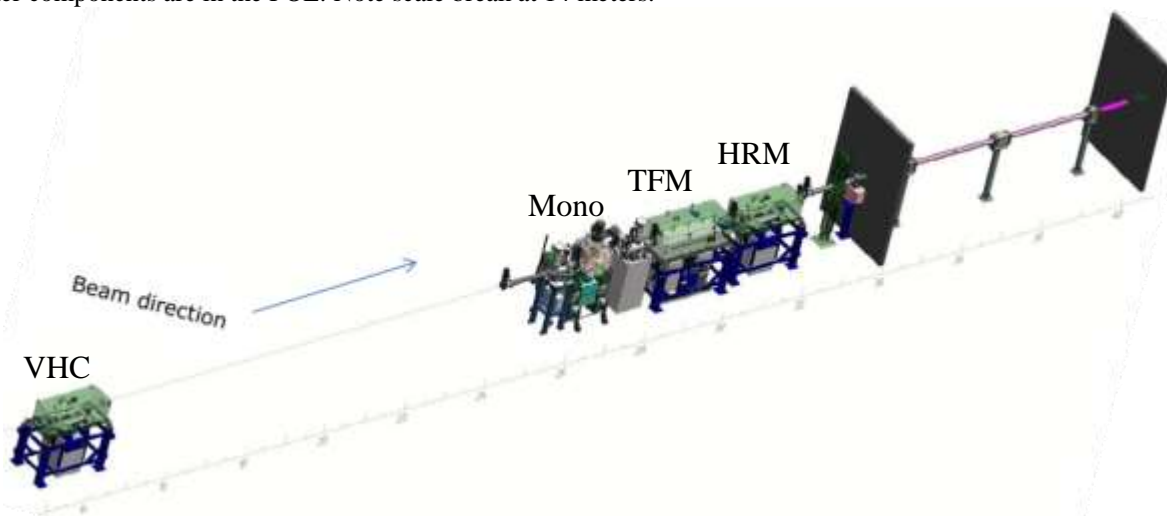


Fig. 1.8: Isometric projection arrangement of beamline optics, showing the VHC in the front end.

Collimating mirror

The first optical element will be a vertically *and* horizontally collimating (VHC) mirror with a paraboloid figure and an optical coating along its length consisting of 5 nm Rh on 30 nm of Pt. This coating allows good performance throughout the entire energy range of the beamline. In particular, the Rh upper coating allows suitable performance through the range of the Pt L edges. (This is discussed further in section 4.5.) This mirror sits inside the shield wall with its center at 13 meters from the source. This allows collection of a large solid angle of beam, thus maximizing flux at the sample.

The first optical enclosure (FOE) houses the following major optical elements:

Monochromator

A double-crystal monochromator, shown in Fig. 1.9, has parallel and perpendicular motion of the second crystal allowing for fixed-exit operation. Both Si(311) and Si(111) crystals are available to the user. The monochromator was delivered with a crystal cage holding a single set of crystals. In the coming year, the crystal cage will be replaced with one offering better cooling and side-by-side placement of both crystal sets. The vacuum vessel will be upgraded to allow translation perpendicular to the beam between the two crystal sets. The Si(311) crystals will enable high resolution XANES and XRD.



Fig 1.9: The BMM DCM, on the floor at Sector 7. Acceptance commissioning with the original crystal cage was performed at X7A at NSLS.

Mirrors

There are two mirrors after the monochromator, a sagittal cylinder bendable along the meridional direction and a plane mirror. The sagittal cylinder will have the same optical coating as the VHC first mirror and will be used to focus the beam only in the horizontal direction or in both the horizontal and vertical directions. Typically, the beam will be focused to a spot for XAS measurements, while for high-

resolution diffraction, either horizontal or no focusing may be used for measurements at the position of the goniometer. The system, however, allows delivery of either focused or collimated beam to either experimental station. The flat mirror will have two different stripes, which are accessible by translating the mirror in the x direction. One will be the same Rh/Pt coating as the first and second mirrors, while the other will be bare Si primarily for rejecting low-energy harmonics. Procurement of these mirror systems is complete with delivery expected in CY2016.

Other Optical Elements

Other optical elements in the FOE include a photon shutter, white beam slits, various masks and monochromatic slits, and an extensive complement of diagnostic equipment.

1.4 End-station

The end station consists of a single hutch. At the entrance to the hutch is the photon delivery termination table. This consists of various diagnostics and a beryllium window all mounted on a vertical translation stage. This motion allows the window and diagnostic elements to follow changes in the beam height in different operating modes for the TFM and the HRM (see Section 2.5).

After the termination table sits an optical table housing a conventional XAS setup of ionization chambers, an energy discriminating fluorescence detector, and various sample stages with sufficient space to install instrumentation for *in situ* or *in operando* measurement. At the downstream end of the hutch sits a six circle goniometer for XRD. The goniometer is used for high resolution XRD measurements as well as XAS experiments in glancing angle, total reflection, and polarization-dependent XAS geometries, in addition to diffraction anomalous fine structure (DAFS). The diffractometer has been obtained by NIST on permanent loan from Robert Sweet of the Photon Sciences Division. Services (power, signaling, water, gas handling, and so on) are tightly integrated into the experimental station in service of efficient, high-throughput XAS and XRD.

Much instrumentation for the XAS station – including silicon drift detectors, ionization chambers, sample stages, a cryostat, computing and communication hardware, and so on – have been transferred from NIST's XAS beamline X23A2 at the NSLS. Most of this hutch equipment is new, with some items, such as the cryostat, dating since 2010.

1.5 Development and Advisory Team

The development team consists of NIST members led by Dan Fischer, and BNL members led by Andrew Broadbent. The team includes Bruce Ravel, Joseph Woicik, Cherno Jaye from NIST along with John Fabijanic and Zhong Zhong from the Photon Sciences Department of BNL.

The NIST staff members represent a permanent and growing investment by NIST in developing and operating beamlines at NSLS-II. Fischer, Woicik, Ravel, and Jaye are scientific staff employed by NIST. The development team has significant and highly successful direct beamline

experience building, developing, maintaining, and managing spectroscopy user facilities, continuously improving measurement capabilities, supporting the development of software for the measurement and interpretation of XAS data, and producing excellent science spanning nearly three decades. They are all highly respected members of the synchrotron community and are valued NIST ambassadors to the DOE at the NSLS-II. The team currently participates in NSLS-II user operations, including the Beamtime Allocation Committee (BAC) and the spectroscopy Proposal Review Panel (PRP), often represents the user community on the NSLS User Executive Committee, and participates in numerous other advisory teams and review panels for NSLS, DOE, and other synchrotron facilities.

The beamline advisory team (BAT) also includes highly regarded scientists within the synchrotron community from various institutions. Each member has significant and highly successful direct beamline experience building, developing, maintaining, and managing spectroscopy or diffraction facilities. The BAT includes:

Simon Bare	SSRL, Chair
Mali Balasubramanian	APS / ANL
Dean DeLongchamp	NIST
Sarbajit Banerjee	Texas A&M University
Andrew Dent	Diamond
Joo Kang	DOW
Tien-Lin Lee	Diamond
Joseph Lienhart	US Army Research Laboratory
Igor Levin	NIST
Tony Olhausen	Sandia
Jose Rodriguez	BNL Chemistry
Stuart Wilkins	NSLS-II / CSX

2 BMM BEAMLINE

We describe in detail the source, front-end, first optical enclosure, and optics including mirrors and monochromators of the BMM beamline.

2.1 Source

The BMM will be sited at port 6-BM of the NSLS-II. A three-pole wiggler (TPW) to be installed at 6-BM will serve as the radiation source for the BMM beamline. The specifications of the three pole wiggler are shown below.

Table 2.1: Three pole wiggler specifications.

Beamline	BMM 6-BM
Type	TPW
Nominal gap	28 mm
Peak field: nominal	1.14 T
Critical energy	6.8 keV
Power total: nominal	250W (TPW) + 69W (BM)
Max. power per unit solid angle: nominal	365 W/mr ²
Device center	366mm U/S of 6-BM-B dipole

Simulation of the spectral flux of the TPW is shown by the dark green line in Fig. 2.1. The simulation assumes a magnetic field of 1.14T, resulting in a critical energy of 6.8 keV at 3.0 GeV ring energy. At 500 mA ring current, the spectral flux is approximately 10^{11} to 10^{13} ph/s/0.1%bw/mrad from 4 to 20 keV.

	Horizontal	Vertical
Size	$\sigma_h = 167 \mu\text{m}$ (FWHM = 393 μm)	$\sigma_h = 12.3 \mu\text{m}$ (FWHM = 29.0 μm)
Divergence	$\sigma_h' = 98 \mu\text{rad}$ (FWHM = 230 μrad)	$\sigma_h' = 0.82 \mu\text{rad}$ (FWHM = 1.9 μrad)

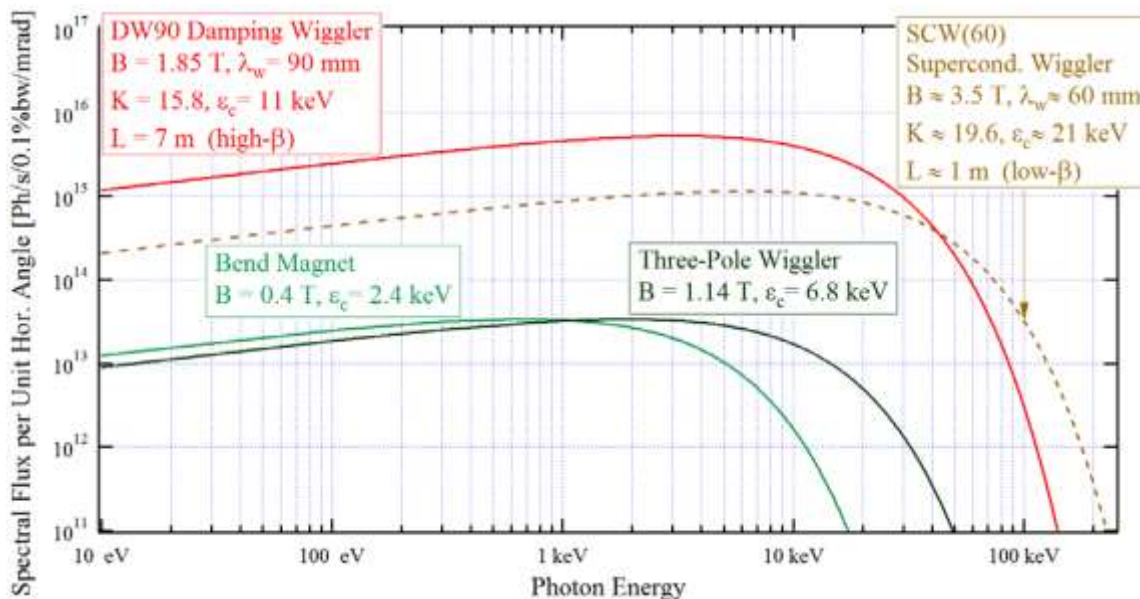


Figure 2.1: Specifications of source size and divergence, and spectral flux of the three-pole wiggler. Electron beam current is assumed to be 500 mA.

2.2 Front End

The front end is also similar to the standard three-pole wiggler front end design, with the opening angle customized to be 0.4 (V) x 3.0(H) milli-radians. Specifications for the front end components are shown in Table 2.2. A collimating mirror, at 13 m from the source, is in the front-end. A Be window is located in the front-end separating the beamline vacuum from the ring vacuum.

Table 2.2: BMM front-end component specifications.

	BMM
Photon shutter (BMPS)	Y
Slow Gate Valve (SGV)	Y
Fixed Mask (FM)	Y
Be Window	Y
Type	Single
Source	3PW

Vertical aperture (mrad)	0.4
Horizontal aperture (mrad)	3.0
Shape	Corner Radius
Bremsstrahlung Collimator BC1	Y
Water Cooled Beryllium Window	Y
Fast Gate Valve (FGV)	N
Number of X-Y Slit sets	1
Mirror System	Y
Fixed Mask 2	Y
Gate Valve	Y
Diagnostics Cross	Y
Photon Shutter (PS)	Y
Bremsstrahlung Collimator BC2	Y
Safety Shutter (SS) (x2)	Y
Cycles per year required	5000
Ratchet Wall Collimator	Y
Gate valve outside Ratchet Wall.	Y

The layout of TPW front end for BMM is shown in Figure 2.2. This design has been adopted for the fixed angle of BMM's VHC mirror, shown in Figure 2.2 in green and labeled "BMM Mirror 1".

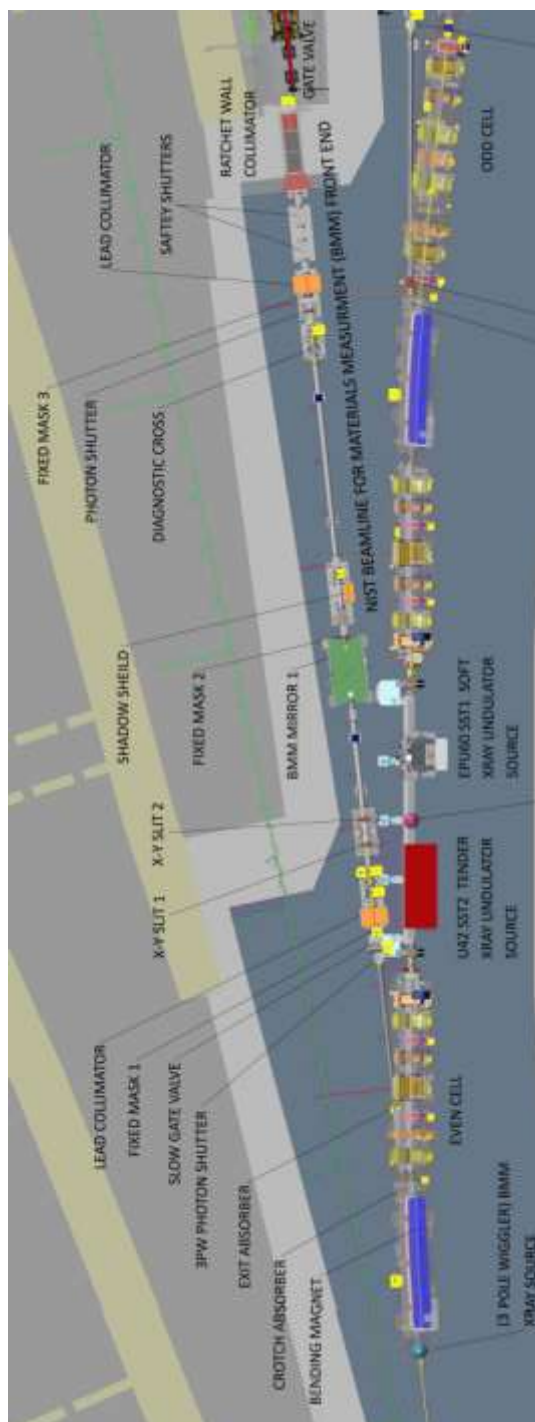


Figure 2.2: TPW front end configuration at NSLS-II. The VHC mirror is shown at 13 m.

Front end beam diagnostics

Beamline diagnostics will begin in the Front End with the integrated beam intensity monitoring on the isolated white beam X-Y slit assembly blades. Additional diagnostic cross downstream of the mirror 1 and upstream of the safety shutter, in the front end can be used to house a retractable water-cooled phosphor panel (and associated camera) in the future as needed.

2.3 Vertical and Horizontal Collimating Mirror

The vertical and horizontal collimating (VHC) mirror system is the first optical component in the BMM beamline, and is located in the front end, inside the shield wall (with the center of the optic at 13 m from the source). The purpose the VHC mirror system is to collimate the beam before sending it downstream to the diagnostic module and the DCM. The VHC mirror is a slot cooled paraboloid and is arranged in a bounce up configuration. The mirror cooling blades sit in an indium-gallium mix located in slots in the optic.

It should be noted that the accelerator tunnel floor inside the shield wall is at a height of 200mm above the experimental hall floor, where the remainder of the beamline is located.

The optic assembly is mounted on in-air lateral translations (one at each end) which allow the optic to be moved laterally in addition to providing yaw adjustment. Vertical translation, pitch and roll are achieved using three in-air vertical jacks mounted on the synthetic granite plinth (two located at one end, one at the other end). The optic assembly is decoupled from the vessel via edge welded bellows. All motors are fitted with encoders for position feedback and limit switches to protect from over-travel.

Table 2.3: Parameters of the VHC mirror. Note that this is a fixed-figure mirror.

Substrate material	Single crystal silicon
Substrate dimensions	1000 mm L x 80 mm W x 60 mm D
Active Area (centered on substrate to within ± 0.5 mm)	900 mm x 30 mm
Grazing incidence angle, P, Q	3.5 mrad (0.2°), 13m, ∞
Substrate Shape	Paraboloid
Tangential slope error	$< 2.5 \mu\text{rad}$ RMS over active length in frequency range L^{-1} to 1 mm^{-1}
Sagittal slope error	$< 25 \mu\text{rad}$ RMS over active length on prepared substrate in frequency range W^{-1} to 1 mm^{-1}
Coating	Rh $50 \text{ \AA} \pm 10\%$ thick on Pt 300 \AA . No binder layers permitted
Surface Roughness	$< 0.3 \text{ nm}$ RMS in frequency range 0.005 to $1 \mu\text{m}^{-1}$. No points over 0.8 nm permitted.
Surface Quality (Scratch/dig)	10-5 to MIL-0-13830A over 99% of surface.
Cooling	Slot Cooled designed for 260 W

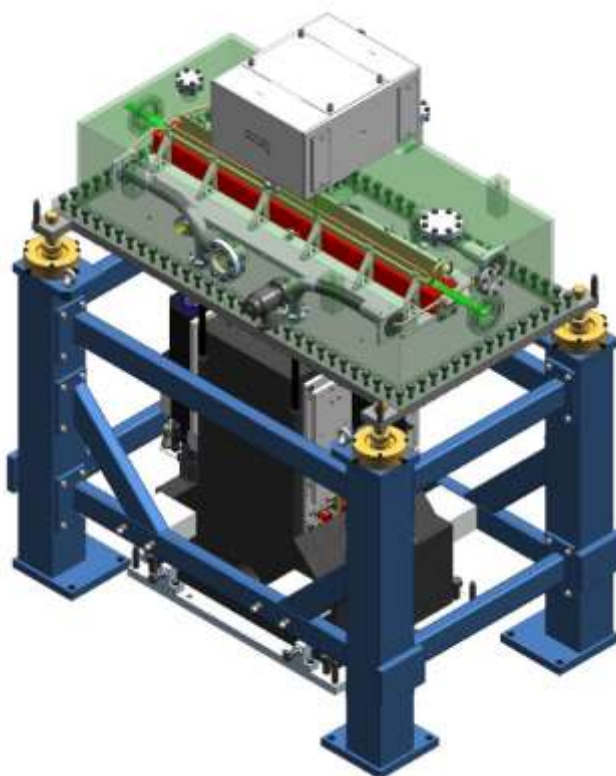


Figure 2.3: Design of the VHC mirror tank

A cooled mask is fitted to the front of the M1 to protect the optic from incident beam. A k-type thermocouple is fitted to the mask to monitor the heat load. Fig 2.4 shows the design of the mask.

The copper cooled mask is inclined to the incoming beam with a 30 degree incidence angle. Beam divergence through the mask is 2 mrad (H) x 0.3 mrad (V). At 13 m from the source, mask receives a maximum beam size of 26 mm horizontal by 3.9 mm vertical. The maximum power density is 365 W/mr^2 . Thus, the maximum power on the mask is 212.4 W. This power load was used for FEA of the mask by FMB-Oxford.

Water is fed to the cooling circuit from outside the vacuum vessel by air guarded hoses that are connected to copper cooling blades. The mirror cooling blades sit in an indium-gallium mix located in recesses in the optic. Water is fed to each cooling circuit from outside the vacuum vessel by air guarded hoses. There are no water-to-vacuum joints.



Figure 2.4: Design of water cooled copper mask for the VHC mirror. The mask, as manufactured, has a U-shaped notch at the entrance to match the figure of the mirror.



Figure 2.5: Design of the VHC mirror cooling that uses cooling blades inserted into eutectic baths in the optic.

The mirror mechanism is mounted on a large plinth, molded from synthetic granite which can be adjusted into its final position using a grouted-in floor plate, which will require pre-alignment.



Figure 2.6: Base assembly with manual adjusters

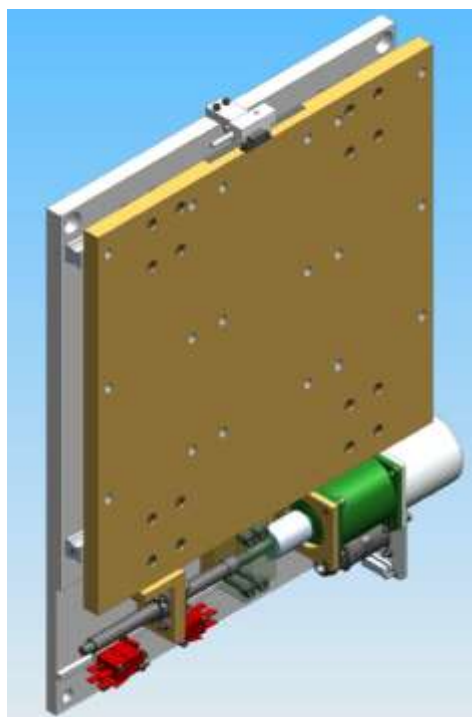


Figure 2.7: In-air lateral translation mechanism, showing location of limit switch

Table 2.4: Motorized motions for M1

Ty Vertical Translation	Movement taken into vacuum via posts fitted with an edge-welded bellows. There is no solid connection between the mechanism and the vacuum vessel.	
	Drive	3 Vertical jacks. 0.1 μ m Encoder
	Range	± 10 mm
	Resolution	<90 μ m
	Repeatability	<2 μ m
	Encoder	Renishaw Tonic-10 mm Pb shielded
Tx Lateral Translation	The lateral translation is made by moving the 2 in air translation stages together.	
	Drive	Lateral slides. 0.1 μ m Encoder
	Range	± 10 mm
	Resolution	<70 μ m
	Repeatability	≤ 2 μ m
	Encoder	Renishaw Tonic-10 mm Pb shielded
Rx Adjustment (Pitch)	Movement made by moving the 2 jacks on one end of the mirror support in opposition with the single jack located at the other end.	
	Drive	3 Vertical jacks. 0.1 μ m Encoder
	Range	$\pm 1^\circ$ (± 10 mm vertically @ 556 crs)
	Resolution	≤ 35 μ rad
	Repeatability	≤ 2 μ rad
	Encoder	Renishaw Tonic
Rz Adjustment (Roll)	Made by moving the inboard jack of one end of the mirror support in opposition with the outboard jacks on the same end of the mirror support. The single jack on the other end of the mirror support is not used for this motion.	
	Drive	2 Vertical jacks. 0.1 μ m Encoder
	Range	$\pm 2.4^\circ$ (± 10 mm vertically @ 240 crs). However, restricted to $\pm 1^\circ$ by roll limit switches
	Resolution	< 1 mrad
	Repeatability	≤ 5 μ rad
	Encoder	Renishaw Tonic
Ry Adjustment (Yaw)	Made by moving the upstream translation stage on one end of the mirror support in opposition with the stage located at the other end.	
	Drive	Lateral slides. 0.1 μ m Encoder

	Range	$\pm 1^\circ$ (± 10 mm laterally @ 556 crs)
	Resolution	$\leq 5 \mu\text{rad}$
	Repeatability	$\leq 2 \mu\text{rad}$
	Encoder	Renishaw Tonic

2.4 First Optical Enclosure

The BMM beamline white beam section, shown in figure 2.8, contains elements conditioning the pink beam coming from the front end, including a filter rack, a Bremsstrahlung stop, a white beam stop.

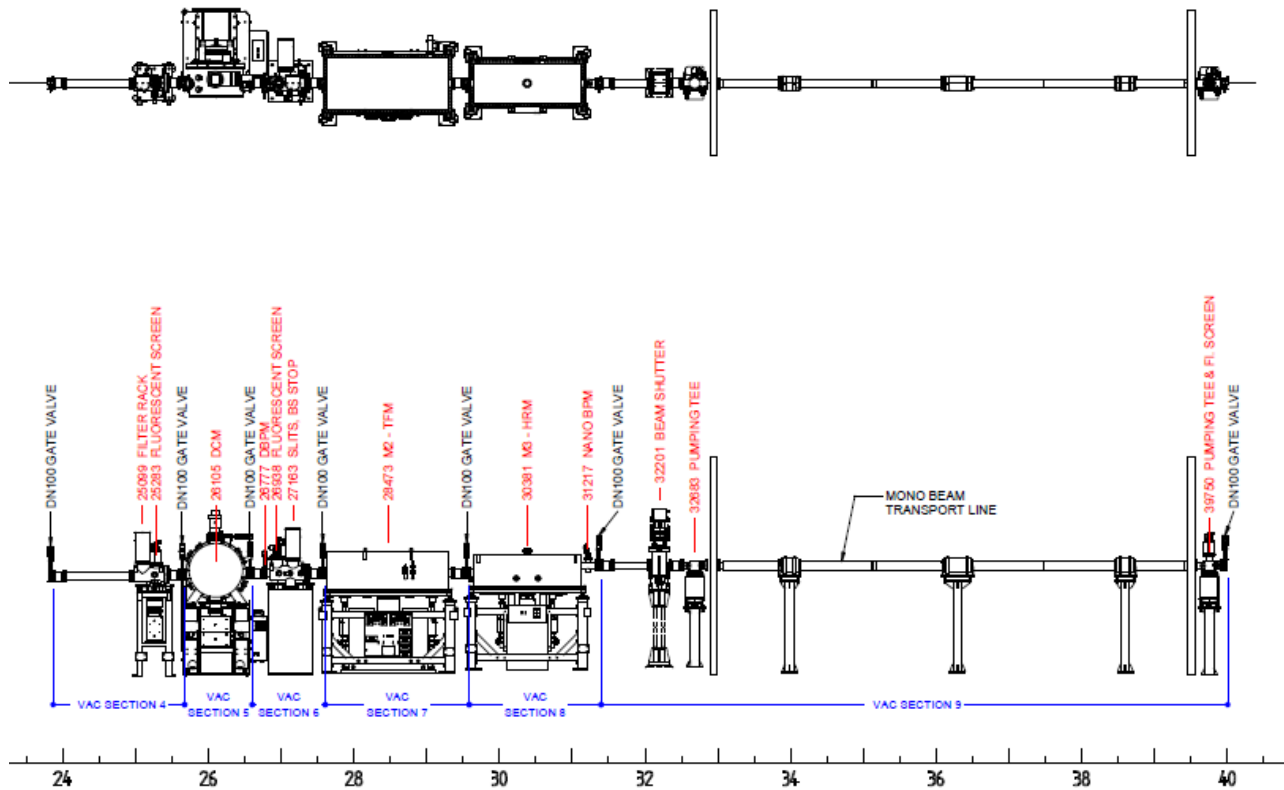


Fig 2.8: Overview of the BMM first optical enclosure.

FOE Beam Diagnostics

Diagnostic Module 1 is located immediately upstream of the DCM and includes a cooled filter unit, photodiode array for measuring scattered radiation (from the filters) and a cooled fluorescent Screen

Diagnostic Module 2 is located immediately downstream of the DCM and includes a pink beam stop, a dual beam-position monitor, a fluorescent screen, a Bremsstrahlung stop, and a 4 blade slit assembly.



Figure 2.9: Diagnostic Module 1



Figure 2.10: Diagnostic Module 2

Shielded Beam Transport Pipe between FOE and Experimental Station

The shielded vacuum tubes have radiation shielding that conforms to existing equivalent radiation standards. FMBO work with Innospec, with whom they have delivered shielded vacuum sections for the Australian Synchrotron and NSLS II.

Table 1.5: Construction of the shielded beam transport pipe

Parameter	Value
Shielding Material	Pb (EN12588)
Vacuum Tube Pb Thickness	7 mm
Pump box Pb Thickness	8 mm
Cover Material	Stainless Steel
Vacuum Tube thickness	0.5 mm
Flange box thickness	2 mm

The steel stands, parts will be painted RAL5007 (FMBO Oxford Standard blue), like other stands on the BMM beamline. Any exposed lead will be painted Flame Red RAL 3000 per BNL specs.

All pipes will have non-rotatable Conflat flanges on the upstream end and rotatable Conflat flanges on the downstream end. Lead collars will be supplied for installation at the exit of the optics hutch and for the entrance of the Experimental Hutch.

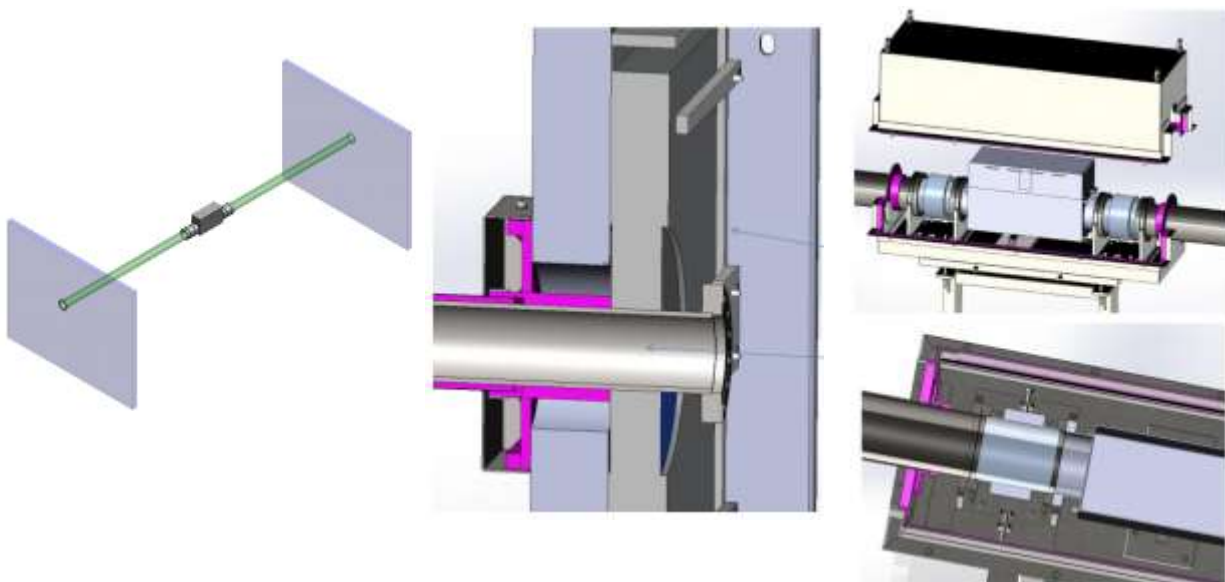


Figure 2.11: (Left) View of flight tube between hutches that will require Pb covers. It is shown here without the Pb covers and pump box and end collars. (Middle) View of the lead collar between the shielded beam tube and the hutch wall. (Right) Detail of the pump box.

The lead box includes tube collars on either end to ensure sufficient lead coverage as shown in the image below. The stands will provide an adjustment of ± 30 mm.

Bellows connecting the shielded tube sections are:

- 200 mm long Stainless Steel Hydroformed Bellows

- Axial and Lateral compliance $\pm 5\text{mm}$

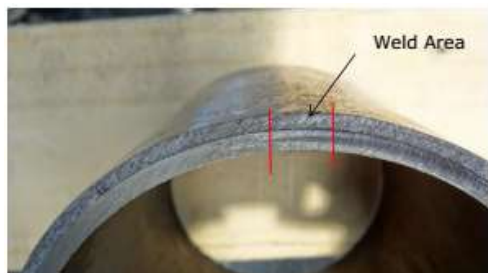


Figure 2.12: No visible inhomogeneous areas in the surrounding of the seam. Lead is closely attached to the tube.

- NW150CF (8" OD) Fixed at upstream end
- NW150CF (8" OD) Rotatable at downstream end

The lead shielded tubes will be manufactured by Innospec. They will be pre-baked in the FMBO factory and sealed, to maintain cleanliness. They will then be delivered to Innospec for lead shielding. The lead shielding is done by forming a shell which fits around the tube and is then welded. A pair of thin, stainless steel shells is then fitted to cover the lead.

Collimators and Beam Stops

All collimators and beam stops will be of standard NSLS-II design and tailored to this beamline in accordance with ray tracing results and shielding guidelines. All collimators will be located in the Front End.

2.5 Beamline Optics

Mirror M1 and the DCM are always in the beam with M1 at an incidence angle of 3.5 mrad, deflecting up. This sets the upper energy cut-off at about 23 keV. The DCM is designed with a vertical offset of 30 mm, bouncing up. The beam exits M1 and the DCM at 7 mrad. The table below describes the 6 modes of operation.

Table 2.6: Description of the 6 operating modes

Mode	Mirrors	Energy	Angle (mrad)	M3 coating	Beam quality
A	M2 only	above 9 keV	3.5		Spot focus (M2 with meridional bend) / line focus (M2 without meridional bend)
B	M2+M3	below 7 keV	5	Bare Si	Spot focus (M2 with meridional bend) / line focus (M2 without meridional bend)
C	M2+M3	below 9 keV	3.5	Bare Si	Spot focus (M2 with meridional bend) / line focus (M2 without meridional bend)
D	M3 only	above 9 keV	3.5	Rh/Pt	Large beam
E	M3 only	below 9 keV	3.5	Bare Si	Large beam
F	M3 only	below 7 keV	5	Bare Si	Large beam

Table 2.7: Vertical heights of key optical elements under different designed operating modes. Note that the locations of the elements marked with gray are approximate and the vertical positions incorrect. This is due to design changes to the beamline following the PDR. Those details will be resolved when the final design of the photon delivery termination table (see Section 3.1) is delivered by the vendor.

Optic	Location	Vertical	M2 only (a)	M2+M3 (b)	M2+M3 (c)	M3 only (d/e)	M3 only (f)	
M1	13000	1400	1400	1400	1400	1400	1400	3.5 mrad for modes (a), (c), (d/e)
DCM	25520	1491.7	1491.7	1491.7	1491.7	1491.7	1491.7	5 mrad for modes (f), (b)
Offset	25520	1521.7	1521.7	1521.7	1521.7	1521.7	1521.7	
M2	28473		1538.3	1538.3	1538.3	1538.3	1538.3	
M3	30381		1538.3	1538.3	1538.3	1551.7	1551.7	
Shutter (upstream end)	31483		1538.3	1520.1	1525.6	1546.2	1546.2	1533.2 average height
FOE Wall (downstream end)	32103		1538.3	1513.2	1520.7	1551.7	1544.1	
ES Wall (upstream end)	37603		1538.3	1447.2	1474.5	1551.7	1524.3	
Gate Valve	38236		1538.3	1442.1	1471.0	1551.7	1522.8	
FS	38406		1538.3	1442.1	1471.0	1551.7	1522.8	
XAFS	40300		1538.3	1417.1	1453.5	1551.7	1515.3	
XRD	44509		1538.3	1387.1	1432.5	1551.7	1506.3	

The following five figures show the beam heights (see Table 2.6) through the beamline in each of the six operating modes. In each figure, the left-most open circle denotes the position of the XRD station. The XAFS station sits 3 meters upstream.

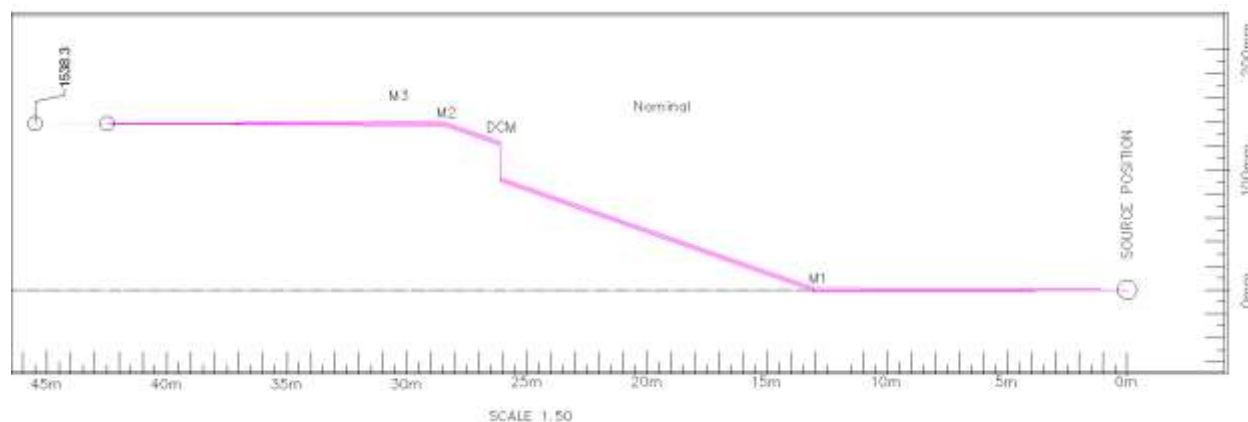


Fig 2.13: Beam propagation under operating mode A, M2 only.

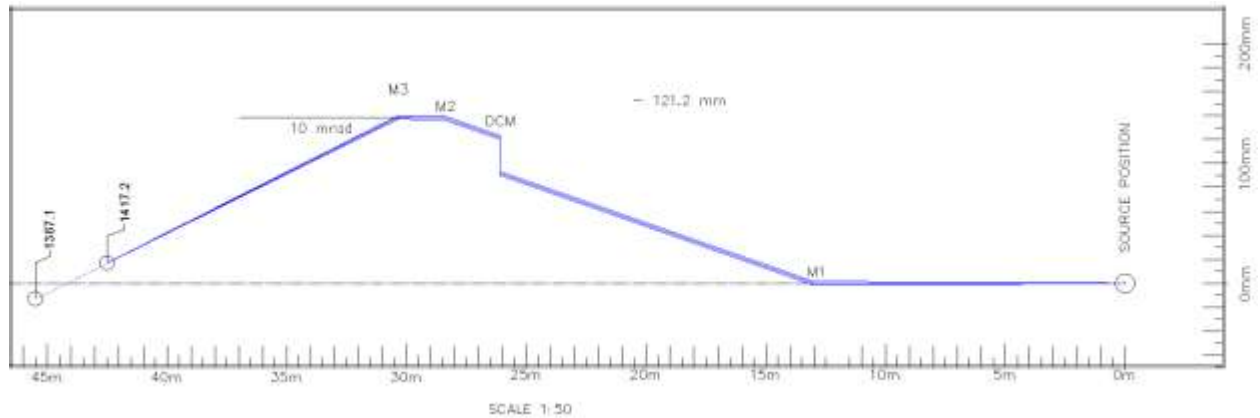


Fig 2.14: Beam propagation under operating mode B, M2 and M3 at 5 mrad.

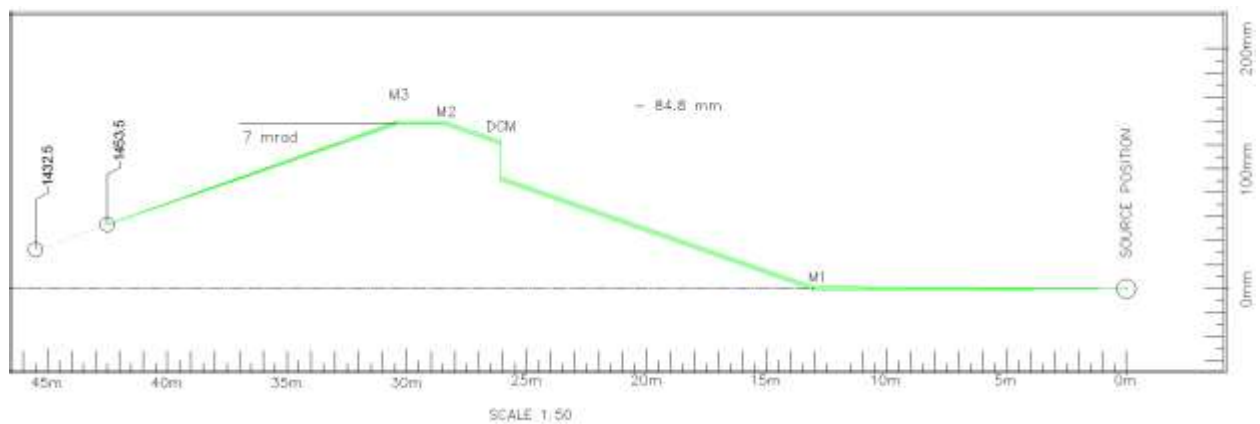


Fig 2.15: Beam propagation under operating mode C, M2 and M3 at 3.5 mrad

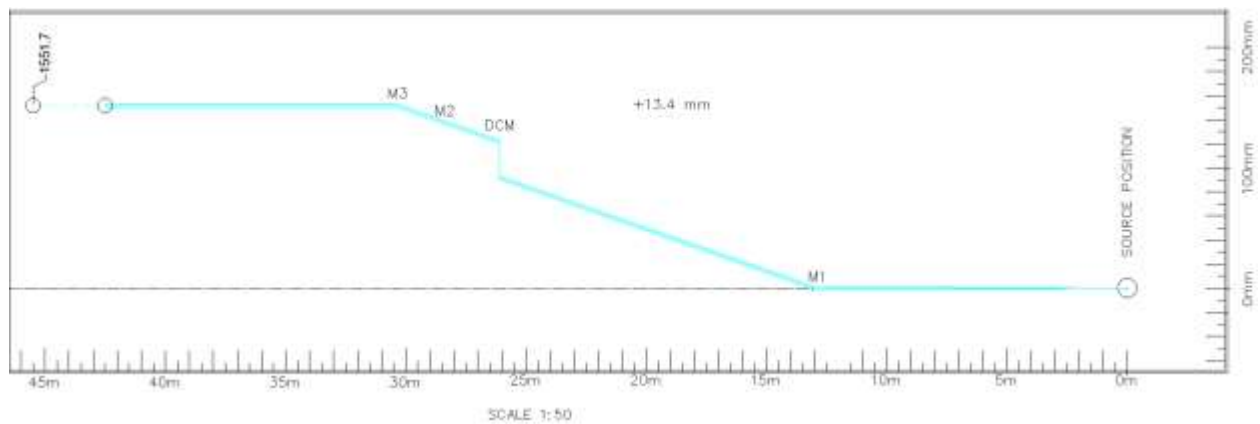


Fig 2.16: Beam propagation under operating mode D and E, M3 only at 3.5 mrad.

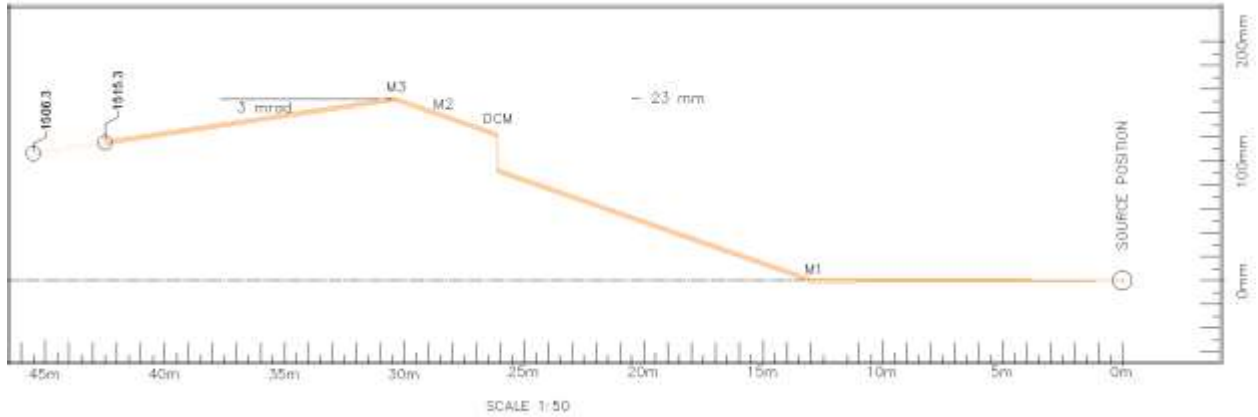


Fig 2.17: Beam propagation under operating mode F, M3 only at 5 mrad.

Table 2.8: Location of BMM beamline components. See Figure 2.8. Note that the locations of elements 27 and 28 are approximate, pending the final design of the photon delivery termination table.

Item	Description	Start (m)	Finish (m)	Vacuum Section
1	Front End 1st section, terminating with gate valve and bellows		12.385	1
2	Paraboloid Collimating Mirror M1	12.385	13.575	2
3	Front End 2nd section, terminating with gate valve in FOE	13.575	23.757	3
4	Bellows	23.757	23.944	4
5	Diagnostic Module 1 with Fluorescent Screen and 2 x 4 Filter Racks and Diode Holder	23.944	24.755	4
6	Gate Valve	24.755	24.825	4
7	Bellows and ZLA	24.825	25.085	5
8	Double Crystal Monochromator	25.085	25.944	5
9	Bellows	25.944	26.216	5
10	Pink Beam Stop	26.216	26.278	5
11	Collimating Tube	26.278	26.657	5
12	Gate Valve	26.657	26.727	5
13	Bellows	26.737	26.833	6
14	Diagnostic Module 2 with DBPM, Fluorescent Screen, Horizontal and Vertical Slits and BS stop	26.833	27.449	6
15	Bellows	27.449	27.555	6
16	Gate Valve	27.555	27.625	6
17	Toroidal Focussing Mirror	27.625	29.400	7
18	Bellows	29.400	29.506	7
19	Gate Valve	29.506	29.576	7
20	Harmonic Rejection Mirror	29.576	31.210	8
21	Gate Valve	31.210	31.280	8
22	Bellows	31.280	31.386	9
23	Beam Shutter	31.386	31.706	9
24	Bellows	31.706	31.816	9
25	Transport	31.816		9
26	Bellows		32.924	9
27	Pumping box with in-line pump	32.924	33.601	9
28	Bellows	33.601	33.801	9
29	Monochromatic beam transport	33.801		9
30	Gate valve		38.271	9
31	Pumping Tee and motorized Fluorescent screen	38.271	38.541	10

32	NanoBPM	38.541	39.105	10
33	In-flange slits	39.105	39.145	10
34	Dual foil intensity monitor	39.145	39.383	10
35	Be window	39.383	39.481	10

Table 2.9: Vacuum design, showing independently pumped vacuum sections.

Maximum bakeout temperature – vessel and internal components	150 °C
Vacuum	UHV compatible, $< 1 \times 10^{-9}$ mbar
Helium leak rate	$< 1 \times 10^{-10}$ mbar l/sec
Outgassing spec-optics not fitted	Masses in the range 38-80 amu shall total $< 1.34 \times 10^{-11}$ mbar.
Vacuum gauges	One Pirani gauge (MKS type 317) and one cold cathode gauge(MKS type 422) located on each vacuum section

The designs of M1 and M3 are shown in Appendix B.

2.6 Monochromator

Power estimates

The power on the first crystal of the monochromator is estimated assuming the operating aperture of 0.4 mrad (V) x 3.0 (H) mrad. The calculations include contributions of 3PW and its adjacent bending magnets. The BM power density is minimum on horizontal center, and maximum near ± 1 mrad (H). The max/min ratio is 1.35. The average of max/min, a factor of 1.18, is applied to the on-axis spectra data supplied by Oleg Chubar. The mirror is coated with 5nm Rh on top of 30 nm Pt, providing a reflectivity of ~ 0.9 below 23 keV.

Power incident on mirror: 88 W
 Power absorbed by mirror: 18 W
 Power after mirror: 70 W

The beam after mirror M1 carries 70 W, which can then be incident on the following filters:

Table 2.10: Filter values

Filter	0.25 mm Be	0.2 mm HOPG	0.5 mm HOPG	0.1 mm SiC + 0.5 mm HOPG
Power after filter	57 W	47 W	38 W	24 W
Intended energy range	<7.5 keV	<10.5 keV	<16.5 keV	>16.5 keV

The power absorbed by the filter can be approximated by the difference in power after the mirror compared to the power after the filter. This represents a slight over-estimate as the scattered x-rays that are not self-absorbed by the filter are ignored.

Note that the first mirror is at 13 m, corresponding to a normal-incidence beamsize of 2.6 mm (V) x 19.5 mm (H). Since the mirror collimates both horizontally and vertically, this beam size is used for FEA of filter and the first crystal of the monochromator.

Finite Element Analysis

FEA of the front end is being performed by FMB-Oxford using the simulated power below for five selected cases.

- Case 1, no filter, 70 W, 55 degrees θ_B (S K edge, Si 111)
- Case 2, no filter, 70 W, 11 degrees θ_B (Mo K edge, Si 311)
- Case 3, 0.25 mm Be filter, 57 W, 50 degrees θ_B , (Ti K edge, Si 311)
- Case 3', 0.25 mm Be filter, 57 W, 24 degrees θ_B (Ti K edge, Si 111)
- Case 4, 0.1 mm SiC +0.5 mm HOPG filter, 24 W, 11 degrees θ_B , (Mo K edge, Si 311)

Here we describe the input configuration for this FEA analysis.

FEA Geometry assumes that horizontal (x) dimension to be 19.5 mm (13 m with 1.5 mrad horizontal operating aperture), vertically (y) to be $2.6/\sin(\theta_B)$ mm, where θ_B is the Bragg angle of the first crystal. y is separated into 11 strips to account for vertical beam non-uniformity.

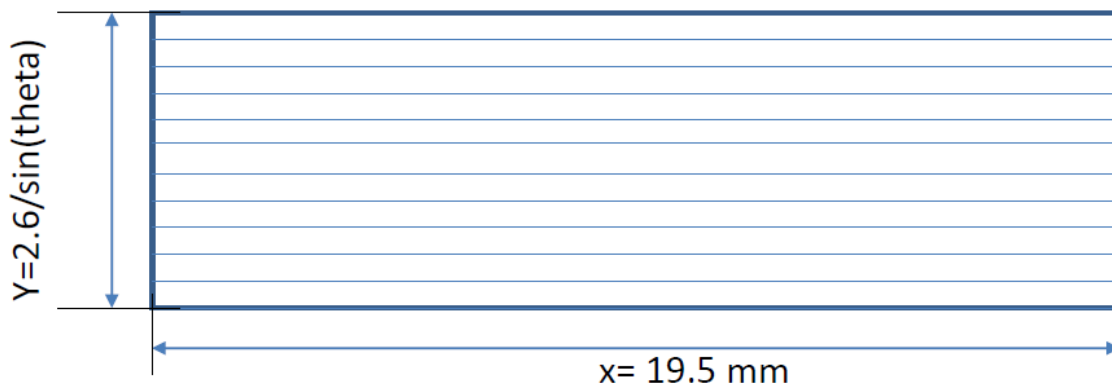


Figure 2.18: Geometry used in monochromator FEA thermal analysis.

Power Density Distribution (integral over all photon energies) from TPW and BM at 30 m

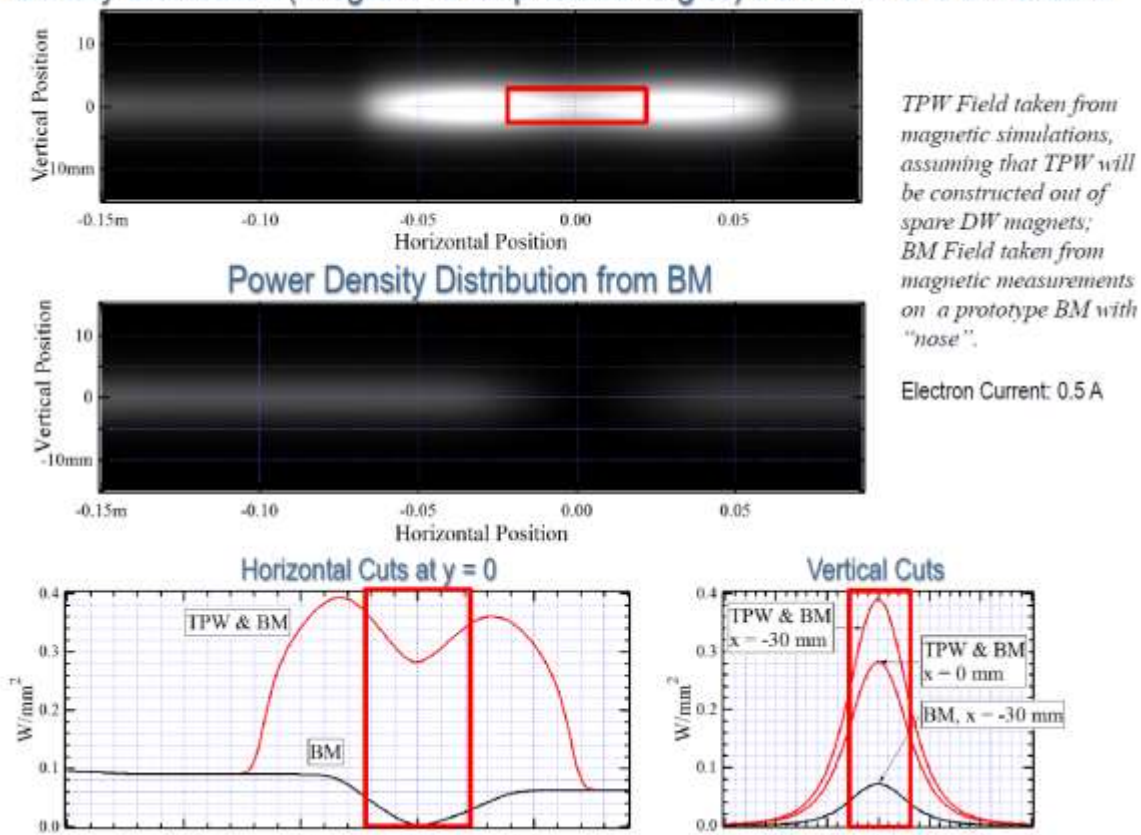


Figure 2.19: Power distribution of the TPW and BM sources

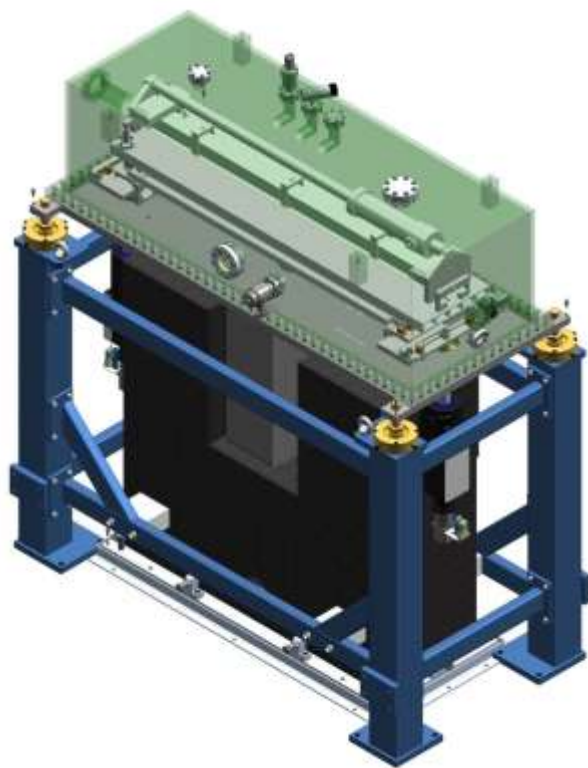
Table 2.11: Power incident upon each segment shown in Figure 12 in each FEA case to be examined.

Case 1	Y (mm)	-1.59	-1.27	-0.95	-0.64	-0.32	0	0.32	0.64	0.95	1.27	1.59
70 W 55°	P (W)	4.5	5.5	6.4	7.1	7.6	7.7	7.6	7.1	6.4	5.5	4.5
Case 2	Y (mm)	-6.81	-5.45	-4.09	-2.73	-1.36	0	1.36	2.73	4.09	5.45	6.81
70 W 11°	P (W)	4.5	5.5	6.4	7.1	7.6	7.7	7.6	7.1	6.4	5.5	4.5
Case 3	Y (mm)	-1.69	-1.36	-1.02	-0.68	-0.34	0	0.34	0.68	1.02	1.36	1.69
57 W 50°	P (W)	3.7	4.5	5.2	5.8	6.2	6.3	6.2	5.8	5.2	4.5	3.7
Case 3'	Y (mm)	-3.19	-2.56	-1.92	-1.28	-0.64	0	0.64	1.28	1.92	2.56	3.19
57 W 24°	P (W)	3.7	4.5	5.2	5.8	6.2	6.3	6.2	5.8	5.2	4.5	3.7
Case 4	Y (mm)	-6.81	-5.45	-4.09	-2.73	-1.36	0	1.36	2.73	4.09	5.45	6.81
24 W 11°	P (W)	1.56	1.89	2.19	2.44	2.60	2.65	2.60	2.44	2.19	1.89	1.56

This power density distribution was provided to Scott Mowatt of FMB-Oxford, who performed FEA analysis of the water-cooled crystal. The results for the FEA is shown below. It shows that the slope error is acceptable for 111 crystal. The slope error is comparable to the Darwin width of 311 crystal at high x-ray energies of about 20 keV. However, we can add additional filters to reduce the heat load at high x-ray energies when 311 crystal is used.

Parameter	Case 1	Case 2	Case 3	Case 3'	Case 4
Edge	S K	Mo K	Ti K	Ti K	Mo K
Energy (keV)	2.471	20.002	4.965	4.965	20.002
Miller indices (Si hkl)	111	311	311	111	311
Angle (°)	55	11	50	24	11
Darwin width (urad)	187.9	5.34	32.66	56.13	5.34
Sagittal size (mm)	19.5	19.5	19.5	19.5	19.5
Tangential size (mm)	3.174	13.626	3.39	4.3923	13.262
Total power (W)	70	70	57	57	24
Max temp (°C)	56.74	41.11	49.11	45.09	28.32
Slope error, tangential (urad)	23.34	15.72	18.35	16.43	5.10
Local slope error, tangential (urad)	1.69	1.30	1.31	1.26	0.40
Fraction of Darwin width	0.01	0.24	0.04	0.02	0.07

2.7 M2: Toroidal focusing mirror



The M2 mirror system is the 3rd optical component in the BMM beamline, and is located immediately downstream of the DCM (with the center of the optic at 28.473m from the source). The purpose the M2 mirror system is to focus the beam vertically and horizontally before sending it downstream directly to the experiment or via M3. It can also be used to deliver beam that is horizontally focused and vertically collimated to the diffraction end station for studies of scattering in the specular plane. It can also be removed from the beam path to allow only M3 to be used. The M2 optic is an uncooled toroid and is arranged in a 3.5 mrad grazing-incidence, bounce-down configuration.

The optic assembly is mounted on two in-vacuum lateral translations (one at each end) which allow the optic to be moved laterally in addition to providing yaw adjustment. Vertical

Figure 2.20: The toroidal focusing mirror.

translation, pitch and roll are achieved using three in-air vertical jacks mounted on the synthetic granite plinth (two located at the beam-exit end, one at the beam-entrance end). Fine pitch is achieved by placing a Digital Piezo Transducer (DPT) in vacuum and in line (series) with the single in-air vertical jack. The optic assembly is decoupled from the vessel via edge welded bellows. All motors are fitted with encoders for position feedback and limit switches to protect from over-travel. The DPT has a strain gauge positional feedback system.

The incident beam height is 1538.3 mm above the experimental hall floor. The optic center is 28.473 m from source. This mirror is vertically deflecting downwards, and vertically and horizontally focusing. Manual adjustments of ± 15 mm in y can be made prior to grouting floor plate. The granite base z, x and Ry (yaw) can then be adjusted from the grouted-in floor plate.



Figure 2.21: In-vacuum lateral translation rails.

The mirror mechanism is mounted on a large plinth, molded from synthetic granite, which can be adjusted into final position using the grouted-in, floor plate which will require pre-alignment.

The vessel shall comprise a stainless steel baseplate onto which is bolted the vessel lid. Access to the mirror is obtained by removing the lid. The vessel shall be rectangular and fabricated from dull polished 304 grade stainless steel plates with full penetration welds and cleaned and prepared in accordance with standard UHV requirements. All flanges shall be Conflats, manufactured from 304 grade stainless steel and sealed with copper gaskets, with the exception of the large rectangular vessel baseplate.

The following three tables outline the optical, motion, and vacuum properties of the M2 mirror assembly.

Table 2.12: M2 optical properties

Operating position	Vertically deflecting downwards, vertically and horizontally focussing
Substrate material	Silicon
Active area	1100 mm x 30 mm
Blank dimensions	1300mmL x 60mmW x 50mmD
Shape	Tangentially flat ($>50\mu\text{m}$), Sagittal Cylinder, bent tangentially to toroid
Incidence Angle, P, Q	3.5mrad, ∞ , 14.027 m
Tangential slope error	$<0.5 \mu\text{rad}$ RMS over active length in frequency range L^{-1} to 1 mm^{-1}
Sagittal Cylinder	$98.2 \text{ mm} \pm 1\%$
Sagittal slope error	$<10 \mu\text{rad}$ RMS in frequency range W^{-1} to 1 mm^{-1}
Coating	Rh 5 nm on Pt 30 nm. No binder layer permitted.
Coating Density	$>95\%$ of bulk material
Surface Roughness	$<0.3 \text{ nm}$ RMS in frequency range 0.005 to $1 \mu\text{m}^{-1}$. No points over 0.8 nm permitted
Surface Quality (Scratch/dig)	10-5 to MIL-0-13830A over 99% of surface.
Cooling	Uncooled

Bender	Cylindrical bender by Thales/SESO
Bending Range	7.5km < R < 40km

Table 2.13: M2 motor motions

Ty Vertical Translation	Movement taken into vacuum via posts fitted with an edge-welded bellows. There is no solid connection between the mechanism and the vacuum vessel.	
	Drive	3 Vertical jacks. 0.1µm Encoder
	Range	±10 mm
	Resolution	<90 µm
	Repeatability	<2 µm
	Encoder	Renishaw Tonic
Tx Lateral Translation	The lateral translation is made by moving the 2 in vacuum translation stages together.	
	Drive	Lateral slides. 0.1µm Encoder
	Range	±10 mm
	Resolution	<70 µm
	Repeatability	≤2 µm
	Encoder	Renishaw Tonic
Rx Adjustment (Pitch)	Movement made by moving the 2 jacks on one end of the mirror support in opposition with the single jack located at the other end.	
	Drive	3 Vertical jacks. 0.1µm Encoder
	Range	±0.8° (± 10 mm vertically @ 722 crs)
	Resolution	≤35 µrad
	Repeatability	≤2 µrad
	Encoder	Renishaw Tonic
Rz Adjustment (Roll)	Made by moving the inboard jack of one end of the mirror support in opposition with the outboard jacks on the same end of the mirror support. The single jack on the other end of the mirror support is not used for this motion.	
	Drive	2 Vertical jacks. 0.1µm Encoder
	Range	±2.4° (± 10 mm vertically @ 240 crs). However, restricted to ±1° by roll limit switches
	Resolution	< 1 mrad

	Repeatability	$\leq 5 \mu\text{rad}$
	Encoder	Renishaw Tonic
Ry Adjustment (Yaw)	Made by moving the upstream translation stage on one end of the mirror support in opposition with the stage located at the other end.	
	Drive	Lateral slides. $0.1 \mu\text{m}$ Encoder
	Range	$\pm 0.8^\circ$ ($\pm 10 \text{ mm}$ laterally @ 722 crs)
	Resolution	$\leq 5 \mu\text{rad}$
	Repeatability	$\leq 2 \mu\text{rad}$
	Encoder	Renishaw Tonic
Rx' (Fine Pitch)	Movement made by moving DPT which is in line with the single jack located at the beam-in end.	
	Drive	$30 \mu\text{m}$ Digital Piezo Transducer (DPT)
	Range	$\sim 40 \mu\text{rad}$
	Resolution	$< 0.05 \mu\text{rad}$
	Repeatability	$< 0.1 \mu\text{rad}$

Table 2.14: M2 vacuum system

Maximum bakeout temperature – vessel and internal components	150°C
Vacuum	UHV compatible $< 1 \times 10^{-9}$ mbar
Helium leak rate	$< 1 \times 10^{-10}$ mbar l/sec
Vacuum pump	Gamma vacuum 500T ion pump located underneath the vessel.
Outgassing spec, optic not fitted	Masses in the range 38-80 amu shall total $< 1.34 \times 10^{-11}$ mbar.
Vacuum gauges	One Pirani gauge (MKS type 317) and one cold cathode gauge (MKS type 422) located on the mirror vessel
Right Angle Valve	VAT Valve type 54, DN40/CF70.

2.8 M3: Planar harmonic rejection mirror

The M3 mirror system is the 4th optical component in the BMM beamline, and is located immediately downstream of the TFM (M2) (with the center of the optic at 30.381m from the source). The primary purpose of the M3 is to provide suppression of harmonic content scattering from the monochromator. It can also be used in place of M2 to direct both vertically and horizontally collimated radiation to the correct location in the hutch, and it can also be removed from the beam path to allow only M2 to be used. The M3 optic is an uncooled plane with selectable Rh or Si stripes. It is a bounce-down mirror intended for a 3.5 mrad or 5 mrad incidence-angle configuration.

The optic assembly is mounted on in-vacuum lateral translations (one at each end), allowing the optic to be moved laterally in addition to providing yaw adjustment. Vertical translation, pitch and roll are achieved using three in-air vertical jacks mounted on the synthetic granite plinth

(two located at beam-exit end, one at the beam-entrance end). Fine pitch is achieved by placing a Digital Piezo Transducer (DPT) in vacuum in line (series) with the single in air vertical jack. The optic assembly is decoupled from the vessel via edge welded bellows. All motors are fitted with encoders for position feedback and limit switches to protect from over-travel. The DPT has a strain gauge positional feedback system.

The incident beam height is 1538.3 mm to 1551.7 mm, depending on whether M2 is in or out of the beam and giving an average height of 1545 mm above the experimental hall floor. The optic center is 30.381 m from source. The operating position is vertically deflecting downwards. Manual adjustments of ± 15 mm are available in y prior to grouting floor plate. Granite base z, x and Ry (yaw) can then be adjusted from grouted-in floor plate.

The mirror mechanism is mounted on a large plinth, molded from synthetic granite which can be adjusted into final position using the grouted in floor plate which will require pre-alignment.

The vessel and in-vacuum translation stage for M3 look very similar to those for M2, so figures are not provided in this section. The following three tables outline the optical, motion, and vacuum properties of the M3 mirror assembly.

Table 2.15: M3 optical properties

Operating position	Vertically deflecting downwards
Substrate material	Single Crystal Silicon
Active area	1100 mm x 65 mm
Blank dimensions	1200mmL x 90mmW x 60mmD
Shape	Plane, R>40km
Incidence Angle, P, Q	3.5 or 5 mrad, ∞ , ∞
Tangential slope error	<0.5 μ rad RMS over active length in frequency range L^{-1} to 1mm^{-1} with >40 km radius removed at ~ 4.8 mm resolution
Sagittal slope error	<10 μ rad RMS in frequency range W^{-1} to 1mm^{-1} with >40 km radius removed
Stripes	Stripe 1: Rh 5 nm on Pt 30 nm, 30mm wide. No binder layer permitted. Stripe 2: Bare Si, 30mm wide
Coating Density	>95% of bulk material
Surface Roughness	<0.3 nm RMS in frequency range 0.005 to $1\mu\text{m}^{-1}$. No points over 0.8 nm permitted
Surface Quality (scratch/dig)	10-5 to MIL-0-13830A over 99% of surface.
Cooling	Uncooled

Table 2.16: M3 motor motions

Ty Vertical Translation	Movement taken into vacuum via a post fitted with an edge-welded bellows. There is no solid connection between the mechanism and the vacuum vessel.	
	Drive	3 Vertical jacks. 0.1 μm Encoder
	Range	± 12 mm
	Resolution	<90 μm
	Repeatability	<2 μm
	Encoder	Renishaw Tonic
Tx Lateral Translation	The lateral translation is made by moving the 2 in vacuum translation stages together.	
	Drive	Lateral slides. 0.1 μm Encoder

	Range	± 35 mm
	Resolution	< 70 μm
	Repeatability	≤ 2 μm
	Encoder	Renishaw Tonic
Rx Adjustment (Pitch)	Movement made by moving the 2 jacks on one end of the mirror support in opposition with the single jack located at the other end.	
	Drive	3 Vertical jacks. 0.1 μm Encoder
	Range	$\pm 1^\circ$ (± 12 mm vertically @ 667 crs)
	Resolution	≤ 35 μrad
	Repeatability	≤ 2 μrad
	Encoder	Renishaw Tonic
Rz Adjustment (Roll)	Made by moving the inboard jack of one end of the mirror support in opposition with the outboard jacks on the same end of the mirror support. The single jack on the other end of the mirror support is not used for this motion.	
	Drive	2 Vertical jacks. 0.1 μm Encoder
	Range	$\pm 2.9^\circ$ (± 12 mm vertically @ 240 crs). However, restricted to $\pm 1^\circ$ by roll limit switches
	Resolution	< 1 mrad
	Repeatability	≤ 5 μrad
	Encoder	Renishaw Tonic
Ry Adjustment (Yaw)	Made by moving the upstream translation stage on one end of the mirror support in opposition with the stage located at the other end.	
	Drive	Lateral slides. 0.1 μm Encoder
	Range	$\pm 3^\circ$ (± 35 mm laterally @ 667 crs) However, restricted to $\pm 1^\circ$ by yaw switches)
	Resolution	≤ 5 μrad
	Repeatability	≤ 2 μrad
	Encoder	Renishaw Tonic
Rx' (Fine Pitch)	Movement made by moving DPT which is in line with the single jack located at the beam in end.	
	Drive	30 μm Digital Piezo Transducer (DPT)
	Range	~ 45 μrad
	Resolution	< 0.05 μrad
	Repeatability	< 0.1 μrad

Table 2.17: M3 vacuum system

Maximum bakeout temperature – vessel and internal components	150 °C
Vacuum	UHV compatible $< 1 \times 10^{-9}$ mbar
Helium leak rate	$< 1 \times 10^{-10}$ mbar l/sec
Vacuum pump	Gamma vacuum 500T ion pump located underneath the vessel.
Outgassing spec, optic not fitted	Masses in the range 38-80 amu shall total $< 1.34 \times 10^{-11}$ mbar.
Vacuum gauges	One Pirani gauge (MKS type 317) and one cold cathode gauge (MKS type 422) located on the mirror vessel
Right Angle Valve	VAT Valve type 54, DN40/CF70.

2.9 Radiation Shielding

First Optical Enclosure

The First Optical Enclosure (FOE) is designed to be white beam compatible and to shield from the Gas Bremsstrahlung (GB) radiation generated in the front end straight section. The specifications for the first optics enclosure in the NSLS-II guidelines, “NSLS-II Guidelines for Beamline Shielding,” were followed for the FOE design and lead thickness specification. Since the Bremsstrahlung shielding requirement overrides the synchrotron shielding requirement, there is no need for extra lead shielding.

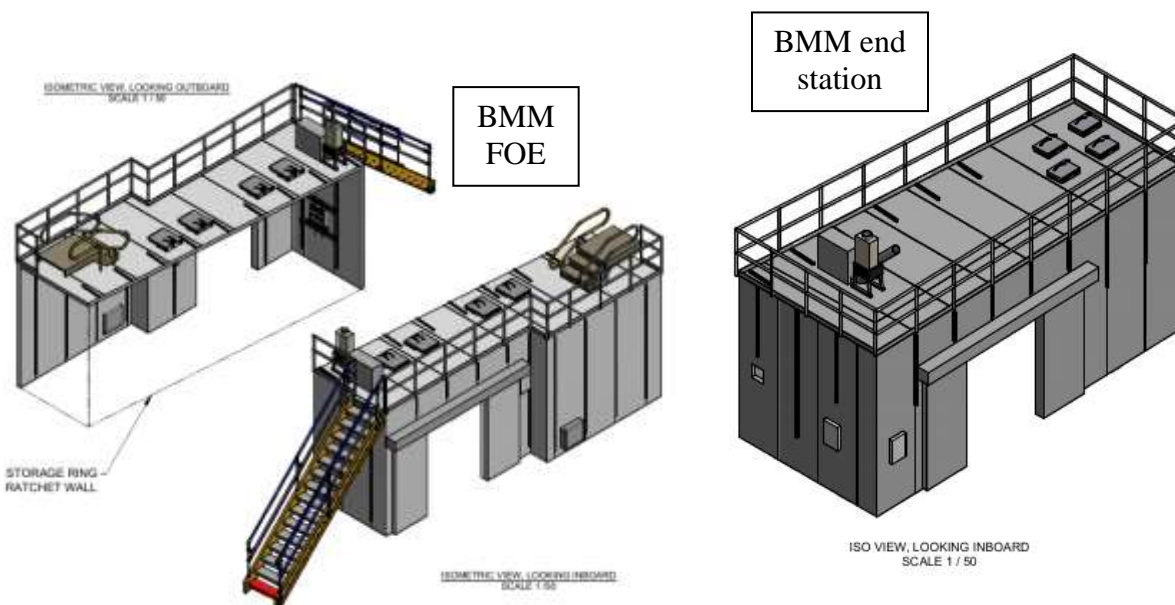


Fig 2.22: Design of the BMM hutches.

The BMM FOE, shown in figure 2.22, is designed with 18 mm-thick lead for the lateral and upstream panels, 50 mm-thick lead for the downstream panel, and 10 mm-thick lead for the roof. The end station and transport pipes are shielded for monochromatic x-rays following NSIS-II guidelines for radiation shielding.

Access to the roof of the FOE is via the roof of the storage ring tunnel or using a staircase from the floor to the downstream end of the FOE (6-BM is a sector required to provide periodic roof access from the floor). Rails are designed to allow personnel access to the roof.



Figure 2.23: The BMM hutches after construction, December, 2015.

Access to the roof of the end station is via a bridge, as shown in Fig. 2.24, from the SST FOE, which in turn can be accessed from the roof of the storage ring tunnel. From the BMM control station, access to the end station roof begins by climbing the staircase to the roof of the FOE, then accessing the storage ring tunnel, walking clockwise to the SST FOE, and then traversing the bridge.



Figure 2.24: The bridge at the downstream end of hutch B providing access to the roof of the end station.

Ray-tracing

The ray-tracing of the BMM beamline is being performed by the FMB-Oxford. This will be based on the BMM front-end ray-tracing provided by the NSLS-II front-end group. Front-end ray tracing can be found in the supplemental materials, pages 9-15.

Secondary Bremsstrahlung radiation shielding

The secondary Bremsstrahlung shields are being designed by FMB-Oxford according to the NSLS-II shielding guidelines. The main scatterers to be considered for Secondary Gas Bremsstrahlung (SGB) shielding analysis are the monochromator first crystal and the white beam stop. A shielded beampipe is placed between the FOE and the experimental hutch. A preliminary SGB design will be proposed using ray-tracing of 2, 4, and 8 degree angles from the straight centerline. We will then ask the radiation safety committee to verify the effectiveness of the proposed secondary Bremsstrahlung shields and shielded

beampipe via Monte-Carlo simulation using the FLUKA code. The simulation results will be used to guide the final design of secondary Bremsstrahlung shields. See supplemental materials for ray tracing.

Synchrotron radiation shielding by the shielded transport pipe

A shielded transport pipe, of 7 mm lead thickness, transports the monochromatic beam from the FOE to the experimental station. Ray-tracing shows that at certain M2 and M3 configurations, the monochromatic beam could strike the shielded transport pipe. The calculations below shows that the 7 mm lead is sufficient to shielded against the monochromatic beam.

The cut-off energy for M1, necessary to bring the beam into the transport pipe, is 23 keV. XOP was used to calculate the reflectivity of Rh-coated mirror at 3.5 mrad design angle. The mirror reflectivity is less than 1% above 40 keV. To be conservative, 100 % reflectivity is assumed for energies below 40 keV, and 1% reflectivity (M) is assumed for energies above 40 keV.

To be conservative, we do not take credit for the Be window, nor the reflectivity of the second and third mirrors. The monochromator is assumed to be the worst-case, Si 111 reflection. IDL program was written to simulate the double-crystal monochromator throughput when the crystals are perfectly tuned to provide maximum output:

$$T = \text{Integrated_reflectivity} * \text{Peak_rocking_curve} / \tan(\theta_B)$$

The results for 7 keV fundamental are shown below.

Reflection	Peak Reflectivity	Integrated Reflectivity (micro-radians)	T (0.1%bw)
111	0.68	46.5	0.107
333	0.77	3.13	0.0082
444	0.78	1.80	0.0048
555	0.76	0.54	0.0014

The worst-case radiation transmission through the shielded lead pipe occurs when the monochromator is tuned close to the M1 cut-off energy. 20 keV fundamental x-ray energy is chosen to represent the worst-case scenario. At 20 keV, the throughput is less than that at 7 keV. Thus the throughput data above is conservative.

Transmission of 7 mm Lead for 20 keV fundamental and its third, fourth and fifth harmonics are then calculated. The results are shown below.

Reflection	E (keV)	μ (1/cm)	Transmission ($\exp(-\mu * t)$)
111	20	978.1	$< 1 \times 10^{-100}$
333	60	55.8	1.1×10^{-17}
444	80	26.8	7.2×10^{-9}
555	100	67.2	8.4×10^{-20}

Using the flux (I) data for 1 horizontal milli-radians, shown in Fig. 2.1, the flux expected in the monochromatic beam, through 7 mm lead is calculated as $2I \cdot T \cdot \exp(-\mu \cdot t) \cdot M$, where the factor 2 accounts for the BMM beam being of 2 milli-radians horizontal divergence. The skin-entry dose rate on water-equivalent tissue is then calculated using the flux rate assuming 1 cm exposure area. The results are shown below:

Reflection	E (keV)	Flux through 7 mm lead (ph/s)	Skin-entry dose rate (mrem/hr)
111	20	$<2.0 \times 10^{-90}$	$<10^{-90}$
333	60	1.8×10^{-10}	2.8×10^{-14}
444	80	6.8×10^{-4}	8.0×10^{-8}
555	100	2.4×10^{-17}	3.4×10^{-21}

To conclude, our simulation shows that the total dose rate for all harmonics is less than 8×10^{-8} mrem/hr, well below the 0.05 mrem/hr guidance for radiation shielding on the experimental floor. We note that the beam will not strike the lead perpendicularly, leading to a path length through the lead that is much larger than the 7-mm considered. The extra attenuation by the steel pipe is not considered to be conservative.

Heatload of the Monochromatic Beam

The ray-tracing of BMM shows that the monochromatic beam, when mis-steered, could be within 1 mm of the stainless steel beam-pipe downstream of the double-crystal monochromator. The maximum flux of monochromatic synchrotron radiation is estimated using the flux (I) data shown in Fig. 2.1. The flux expected in the monochromatic beam is $2I \cdot T \cdot M$, where the factor 2 accounts for the BMM beam being of 2 milli-radians horizontal divergence. At 7 keV, the monochromatic beam flux is 10^{13} ph/s. The maximum power of the monochromatic beam is thus 1.1×10^{-2} Watts. This power is thermally safe for the stainless steel beampipe. The beampipe is located in the FOE that provides adequate shielding for the synchrotron white beam, thus there is no radiological concern for the monochromatic beam striking beampipe in the FOE. Thus we conclude that it is both thermally and radiologically safe for the BMM monochromatic beam to strike the beampipe in the FOE.

3 END STATION

The BMM end station is a large, trapezoid-shaped enclosure housing an optical table in the upstream half of the hutch and serving as the XAFS end station and a goniometer in the downstream half. Along the beam path, the end station is 8 meters long. At the downstream end, the end station is 3.5 meters wide, narrowing to 2.772 meters at the upstream end. This unusual shape is imposed upon the end station in order to fit within the access walkways on either side. This location along the beam path was chosen to provide good performance from the TFM while leaving extensive open floor space downstream of the end station. This open space will be put to good use by BMM and SST for control stations, storage, and space for sample preparation and staging.

3.1 End station diagnostics

The first item in the end station is the photon delivery termination table, Figure 3.1. This consists of a beryllium window containing the final vacuum section of the beamline. This window is mounted on the downstream end of a diagnostic module consisting of a fluorescent screen just inside the hutch. This has motorized motion to follow the height of the incident beam in the various modes (see Section 2.5).

Following the fluorescent screen are the joining bellows, a NanoBPM, a set of 4-blade slits, an intensity monitor, and finally the uncooled Be window. These are mounted on a vertical translation stage that moves all these elements up and down to follow the different beam configurations.

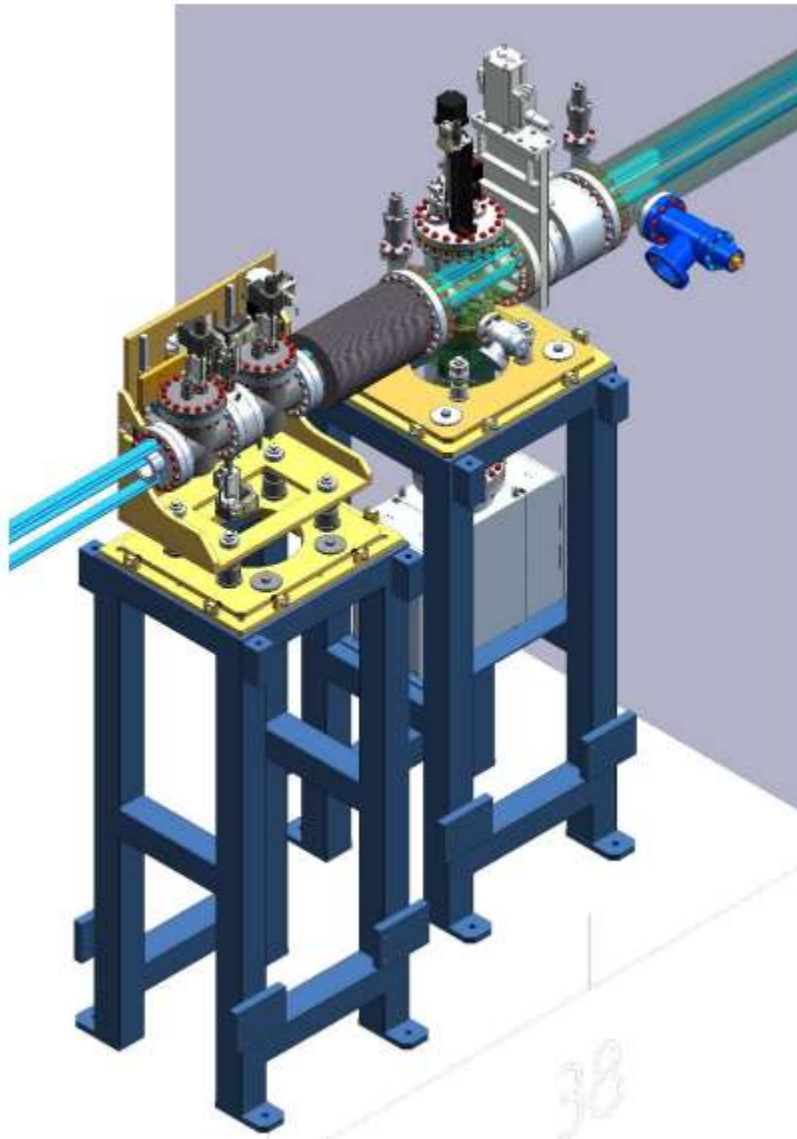


Figure 3.1: Photon delivery termination table

Together, these various elements allow extensive tools for beamline characterization, as well as several elements that can be used for active feedback to control the positions of the monochromator second crystal, M2, and/or M3.

32. Nano beam position monitor

The NanoBPM shown in Fig. 3.2 is a single device that can measure (in-situ) beam position and shape. The technology behind the Nano-BPM is exclusively licensed by FMB Oxford from the University of Manchester. [The novel X-ray beam characterization technique](#) was developed by Dr Roelof van Silfhout.

At the core of the Nano-BPM is a thin foil of an amorphous low-Z type material that is placed in the X-ray beam at 45° . A small amount of radiation is elastically scattered from the polyimide foil and detected by an X-ray camera system that is placed at right angles with the beam. The camera system is constructed in such a way that a magnified image of the beam is recorded and the magnification factor can be changed easily. An innovative aperture design allows sufficient flux to be recorded by the sensor for high-resolution beam sensing even in the case of bending magnet beam lines. This method was filed for patent protection in July 2008. The key innovation of the Nano-BPM technology is its capability to magnify any beam movements at the sensor



Figure 3.2: NanoBPM assembly

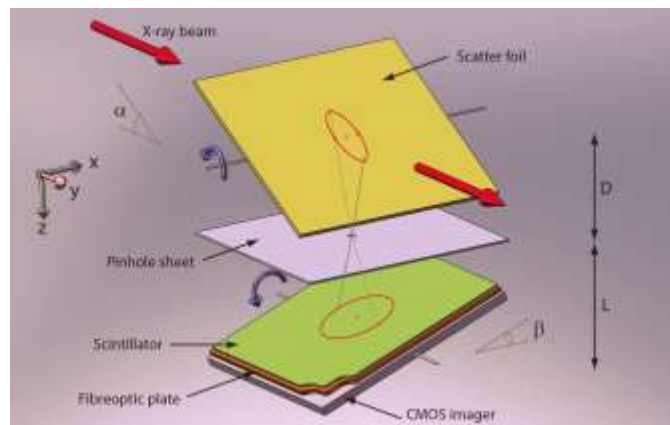


Figure 3.3: Schematic of NanoBPM operation

position as shown in figure 3.3. Small changes (δz) in the centroid position of the incident X-ray beam produce a magnified position movement at the detector of Δy .

Table 3.1: NanoBPM in-air actuator

Motor Type	Nanotec Bipolar 2 phase stepper motor with manual knob
Step angle (full step drive)	1.8°/200 steps/rev
Driving current	1.4 A (max)
No. of 1/2 steps/revolution	400
Drive type	Direct-bellows sealed
Resolution per full step	5 μm
Maximum movement	25 mm
Connector	12-Way Trim Trio
Readhead type	MQPO0122-(Renishaw T1001-05A)
Readhead resolution	0.1 μm
Scale type	MQPO0111-20 μm (Renishaw RGSZ20)
Precision reference type	MQPO0098-(Renishaw A-9653-0143)
Interpolator	MQPO0109 (Renishaw Ti0200E04A)
Connector	15-Way sub D

3.2 XAFS End station

The XAFS end station will consist of an articulated optical table with several translational and rotational degrees of freedom allowing for alignment of the table with the incident beam in any of the operation modes of mirrors M2 and M3. This will require about 150 mm of vertical travel to accommodate the vertical displacement of the beam among the various modes. Additionally, a few degrees of rotation in pitch and yaw will allow alignment of detectors, the axes of the sample stages, and any sample environments with the beam flight path in the various modes. While this will often result in the surface of the table not being completely perpendicular to gravity (i.e. round things might roll along the table top), this method of table alignment simplifies the alignment of specialized sample enclosures (for example, our cryostat) with the actual beam path.

The optical table will house a standard complement of XAFS instrumentation, most of which is repurposed from use at X23A2. This includes a heavy-duty XYZ stage which serves as the main sample positioner and a full complement of sturdy, low-noise ionization chambers. We have a variety of additional motors and X-rail hardware for setting up other parts of the experiment. We have four- and one-element silicon drift detectors along with a complete set of very fast, analog electronics for readout. The excellent performance of the four-element drift detector for XAFS studies together with its dead-time correction algorithm has been described in detail by our group: [Woicik et al., J. Synchrotron Rad. 17, 409 \(2010\)](#). In addition, we are watching the development of fast digital technologies (such the Quantum Detectors Xpress 3) in order to develop a microns-scale fluorescence mapping and μ -spectroscopy capability at BMM.

Also being repurposed from BMM is a host of instrumentation for specialized XAFS measurements, such as:

- High-precision tilt and rotation stages for polarization-dependent surface and thin film studies
- A low-vibration cryostat for a wide variety of materials science and other studies, including orientation sensitive work on thin films

- Polycapillary optics and a diamond incident flux sensor for use with tiny samples or for XRF mapping and μ -spectroscopy with 30 μ m spatial resolution
- Multichannel ionization chambers for use with the wide beam of modes D, E, or F (see Table 2.6 and following) allowing for parallel XAS measurements or combinatorial screening of samples

The end station will have a full complement of utilities, including compressed air, liquid nitrogen, and gaseous nitrogen. This will enable a wide variety of specialized instrumentation such as a cryopump, anoxic sample environments, and others. Along with ventilation and lecture bottles of experimental gases, BMM will support a wide variety of *in situ* and *in operando* chemistry experiments. A future upgrade to hook into the industrial gas handling system being implemented at the ISS beamline at 8-ID would enhance the chemistry mission of the beamline.

Because the optical table will be a large, open surface accommodating a wide variety of beamline-curated and user-supplied instrumentation, the XAFS end station will support the full breadth of the XAFS program which has developed at NSLS over the last three decades while also fulfilling NIST mission needs in hard X-ray spectroscopy.

3.3 Diffraction End station

The XRD end station is a six-circle Ψ diffractometer belonging to the old Protein Crystallography Research Resource (PXRR). It had been used at NSLS beamline X25 and was obtained on permanent loan from BNL's Bob Sweet. It is currently stored along with other NIST instrumentation on the floor at NSLS-II and will be installed in the end-station some time in 2016.

In addition to bicron detectors, the goniometer is also equipped with a HERMES-based photon-counting silicon monostrip detector obtained from the BNL Instrumentation Division for high throughput and high resolution reciprocal space mapping. This detector is 800 mm and 640 pixels long with 30 msec readout and manages up to 10^5 counts per second in photon-counting mode. A future upgrade will be to procure a photon-counting pixel-array detector for rapid data collection and pair-distribution function analysis.



Figure 3.4: Six circle Ψ diffractometer in operation at NSLS beamline X25.

A new Pilatus 100K photon counting area detector was procured in 2015 by NIST's partners at IBM to complement the existing point and strip detectors. This area detector can also be deployed for a number of spectroscopic applications, including full-field transmission XANES, constant-momentum-transfer measurements, and X-

ray emission spectroscopy.

The XRD end station will be used in different ways in three of the operation modes of mirrors M2 and M3. In the high resolution vertical scattering plane mode, the vertical collimation and horizontal focusing will enable high-resolution studies of specular scattering from surfaces and thin film samples. In the high

resolution out-of-plane mode, the large beam will be collimated in both directions, enabling high-resolution studies of scattering in any direction, including in-plane diffraction, to study thin-film growth, coherence, and strain. This mode will also take advantage of the full six axes of the goniometer. In the fully focused mode, the spot focus allows for simultaneous measurement of XAFS with low-resolution XRD. This mode will also enable XAFS measurements at constant momentum transfer q (such as reflectivity XAFS or DAFS) or polarized XAFS studies with any sample orientation. Ruben Reininger's report on reducing the beam divergence and suppressing higher orders at the BMM beamline is included in Appendix A.

Like the XAFS end station, the XRD end station will benefit by the full complement of services and utilities available. The same wide variety of specialized sample environments and *in situ* or *in operando* measurement will be available for high-resolution XRD or combined XRD/XAFS studies.

3.4 Beamline Utilities

The FOE and end station will have the standard suite of utilities including electrical power, liquid nitrogen, DI water and process cooled water, compressed air, and exhaust and ventilation. See Fig 3.5 for pylon locations distributing utilities to the end station and to the work area downstream of the end station.

Table 3.2: Water requirements for the FOE and end station. Note that DI water must have conductance between 3 $\mu\text{S}/\text{cm}$ and 14 $\mu\text{S}/\text{cm}$ and a pH between 7 and 7.5.

Location	Items	Type	PPS/EPS	Nominal flow rate	Warning trip flow rate	Minimum (shutdown) flow rate.
Front end	Mask	DI	EPS	0.5 gpm	0.375 gpm	0.25 gpm
Front end	Mirror optic	DI	EPS	0.5 gpm	0.375 gpm	0.25 gpm
FOE	first diagnostic module, filter and fluorescent screen, in series	DI	EPS	0.5 gpm	0.375 gpm	0.25 gpm
FOE	monochromator	DI	EPS	1.0 gpm	0.375 gpm	0.25 gpm
FOE	pink beam stop	DI	PPS	0.5 gpm	0.375 gpm	0.25 gpm
FOE roof	Motor control rack on roof,	PCW		1.25 gpm/rack		
Floor between hutches	Vacuum rack,	PCW		1.25 gpm/rack		
End station roof	Three racks on roof	PCW		1.25 gpm/rack		
End station	2 drops at XAS station and XRD	PCW		2 gpm for the E.S.		

	station					
Control station	1 rack	PCW		1.25 gpm/rack		
Sample prep area	1 drop in sample prep area	PCW		2 gpm nominal		

Table 3.3: Compressed, air, GN₂, and LN₂ requirements for the FOE and end station.

Location	Use	Type	Number
FOE	Gate valves	Compressed air	7
FOE	Screen in DM1	Compressed air	1
FOE	Photon Shutter	Compressed air	1
FOE	Vacuum bleed-up	GN2	1
End station	Gate valve	Compressed air	1
End station	Screen in DM3	Compressed air	1
End station	Experiment	Compressed air	2
End station	Experiment	GN2	2
End station	Experiment	LN2, standard valved drop	1
Sample prep area	Experiment	Compressed air	1
Sample prep area	Experiment	GN2	1

List of components requiring compressed air

1. FOE
 - 7 gate valves
 - fluorescent screen in diagnostic module 1
 - 1 photon shutter
2. End station
 - 1 gate valve
 - fluorescent screen in photon delivery termination module
 - 2 drops, XAS station and XRD station
3. Downstream of end station: Control station and Sample preparation area
 - 1 drop at sample prep area

List of components requiring GN2

1. FOE
 - 1 drop for dry bleed up of vacuum sections (located on inboard wall, in downstream half of the hutch).
2. End station
 - 2 drops, XAS station and XRD station
3. Downstream of end station: Control station and Sample preparation area
 - 1 drop at sample prep area

List of components requiring LN2

1. End station
 - 1 standard valved drop between XAS station and XRD station

Electrical power, summarized

FOE (Panel 1):

1. Rack on roof: 2 x 20A 110V power circuits + 1 UPS circuit
2. Rack on floor: 2 x 20A 110V power circuits + 1 UPS circuit
3. 3 outlet strips: 2 x 20A 110V power circuits
4. 1 3-phase outlet, 3 circuits

9 circuits + 2 UPS circuits

End Station (Panel 2):

1. 3 Racks on roof: 6 x 20A 110V power circuits + 3 UPS circuits
2. 5 power strips inside hutch distributed over 3 circuits: 3 x 20A 110V power circuits
3. 1 strip on roof, one on wall: 1 x 20A 110V power circuit
4. 3-phase outlet in hutch: 3 circuits
5. 2 strips in sample prep area: 2 x 20A 110V power circuits
6. 3-phase outlet in sample prep area: 3 circuits
7. 208 power inside hutch: 1 x 208V / 30A outlet (2 circuits)
8. 208 power in sample prep area: 1 x 208V / 30A outlet (2 circuits)

22 circuits + 4 UPS circuits (3 racks, 1 drop in sample prep area)

Power needs itemized

Racks

- 1 on roof of FOE (motors)
- 1 downstream of FOE (vacuum)
- 3 on roof of End Station (2 motors, 1 vacuum)
- 1 in control area (motors/electronics)

Each rack should have a standard package for power, including

- 2 x 20A 110V power circuits
- 1 x 15A 110V UPS power
- 2 smart strips for sequential start-up of instruments

This accounts for 6 racks, 2 breakers per rack, excluding UPS.

- Panel #1 on mezzanine provides power for all outlets and equipment in and on the FOE and outlets/equipment between hutches.
- Panel #2 on end station provides power for all outlets and equipment in and on the End station and outlets/equipment in the control area and the sample prep area.

The following covers all other power requirements beyond that needed for racks

110 volts

1. A hutch
 - 4 strips of 6 outlets inside FOE (2 circuits)
 - 1 strip of 4 outlets on FOE roof, 1 strip of 6 outlets on downstream, exterior wall (could be under stairs). (1 circuit).
2. B hutch
 - 5 strips of 6 outlets inside hutch (3 circuits)
3. Downstream of end station: Control station and Sample preparation area
 - 1 strip on exterior, downstream wall of hutch (1 circuit)
 - 2 strips in sample prep area (2 circuits)

3 phase

1. FOE
 - 1 outlet, downstream/outboard corner (3 circuits)
2. End station
 - 2 outlets, inside hutch, on inboard wall, between XAS and XRD stations (6 circuits)
3. Downstream of end station: Control station and Sample preparation area
 - 1 outlet (3 circuits)

208 V

1. End station
 - 1 x 208V / 30A outlet inside hutch, on inboard wall, between XAS and XRD stations (2 circuits)

- 1 x 208V / 30A outlet (2 circuits)

- One drop in control area
- One drop in B hutch

The NSLS-II standard ventilation system is employed for both hutches, comprising a fan on the roof of the hutch, and labyrinth and an air sock on the ceiling to distribute air without drafts. A maximum air exchange rate of 6 air changes per hour is possible, with the flow rate being adjustable by the staff to minimize noise or vibration.

The end station is fitted with a single exhaust labyrinth which will be connected to the facility gas extraction system. This can be used for ventilation of exhaust gases and small quantities of toxic gases (subject to approval in a safety approval form).

The Equipment Protection System (EPS) consists of sensors as tabulated in Table 3.4, following the vacuum section diagram in Figure 3.5



Vacuum section	Vacuum gauge	Ion pump	Gate valve	Flow sensor	Thermocouple
1*	Front end section #1				
2	1	1	1	1	3
3*	Front end section #2				
4	1	1	1	3	9
5	1	1	1	1	7
6	1	1	1	0	0
7	1	1	1	0	2
8	1	1	1	0	2
9	3	2	1	0	0
Total	9	8	7	5	23

Table 3.4: EPS components in each vacuum section. Note that vacuum sections 1 and 3 are sections of the standard 3PW front end. EPS requirements for the front-end sections are not tabulated here. Also note that 1 vacuum gauge and 1 ion pump (vacuum section 2) are in the front end and that one gate valve is controlled by the front end.

Additional EPS components:

1. Extra solenoid wiring needed in vacuum sections 4 and 6 for fluorescent screen insertion (2 x 24V)
2. Water leak detection in FOE

3.6 Personnel Protection System

The Personnel Protection System (PPS) consists of components tabulated in Table 3.5, following the vacuum section diagram in Figure 3.6.

Personnel Protection System (PPS) components related to the FOE will be based on standard NSLS-II FOE design. The FOE PPS includes a set of redundant sensors and interlocks for the cooling water of the critical white beam components (beam collimator and stop), and a separate set of interlocks for the monochromatic beam shutter. It also includes interlocks for the user labyrinths in both hutches as well as door switches, locks and the search and e-stop buttons.

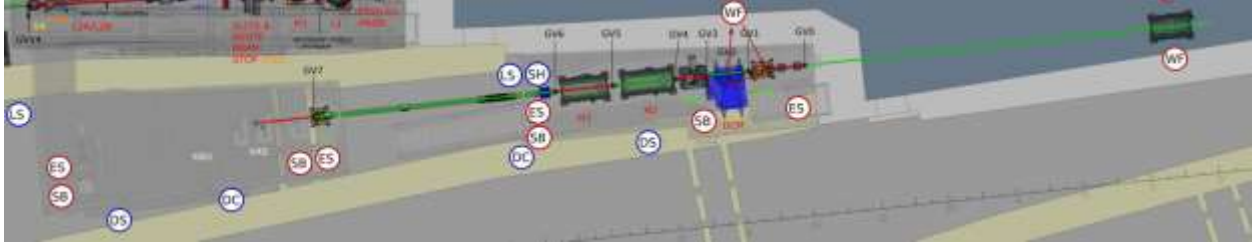


Figure 3.6: Markup of BMM showing locations of PPS components.

Acronym	Meaning	FE	FOE	ES
WF	Water flow	1	1	
SB	Search button		2	2
ES	Emergency stop button		2	2
DC	Door control		1	1
DS	Door switch		1	1
SH	Shutter for monochromatic beam		1	
LS	Labyrinth switch		1	1

Table 3.5: PPS components with locations marked in Figure 3.6.

3.7 Laboratory Space and Access

Laboratory space for SST in room 3LL04 is shared with three other beamlines (IXS, SIX, and ISR). Laboratory space for BMM in room 3LL02 is also shared with three other beamlines (ISS, TES, and QAS). A dedicated laboratory for NIST activities is desirable.

3.8 Work Area

The main control area for the BMM will be downstream of the experimental hutch. A preliminary layout is shown in Figure 3.7. Note that permission will be sought from NSLS-II management to divert the egress aisle as indicated in the figure.

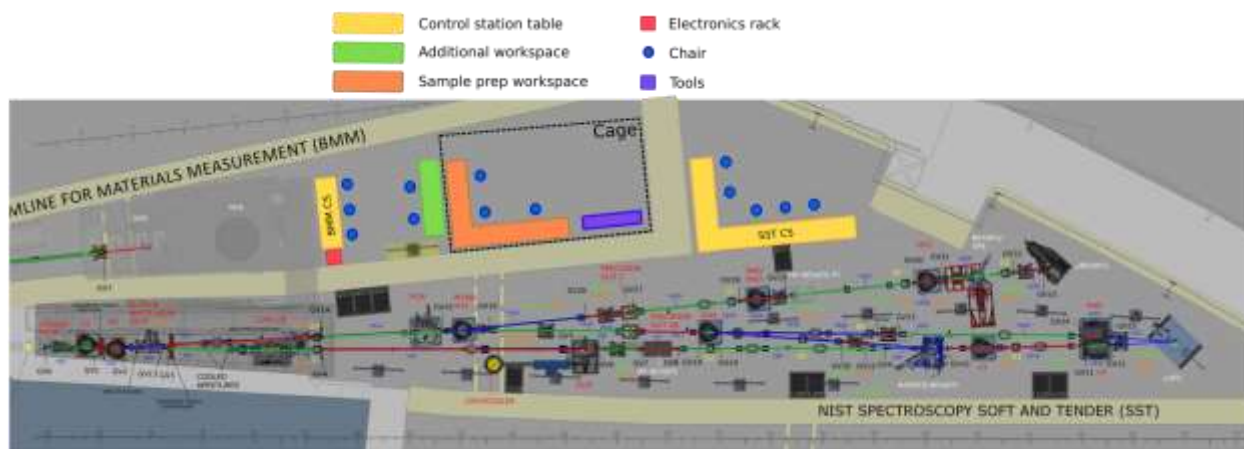


Figure 3.7: A rough sketch of the 6BM and 7ID work area. Note that the lift at the downstream end of the 6BM floor space was removed in May 2016 and filled with concrete.

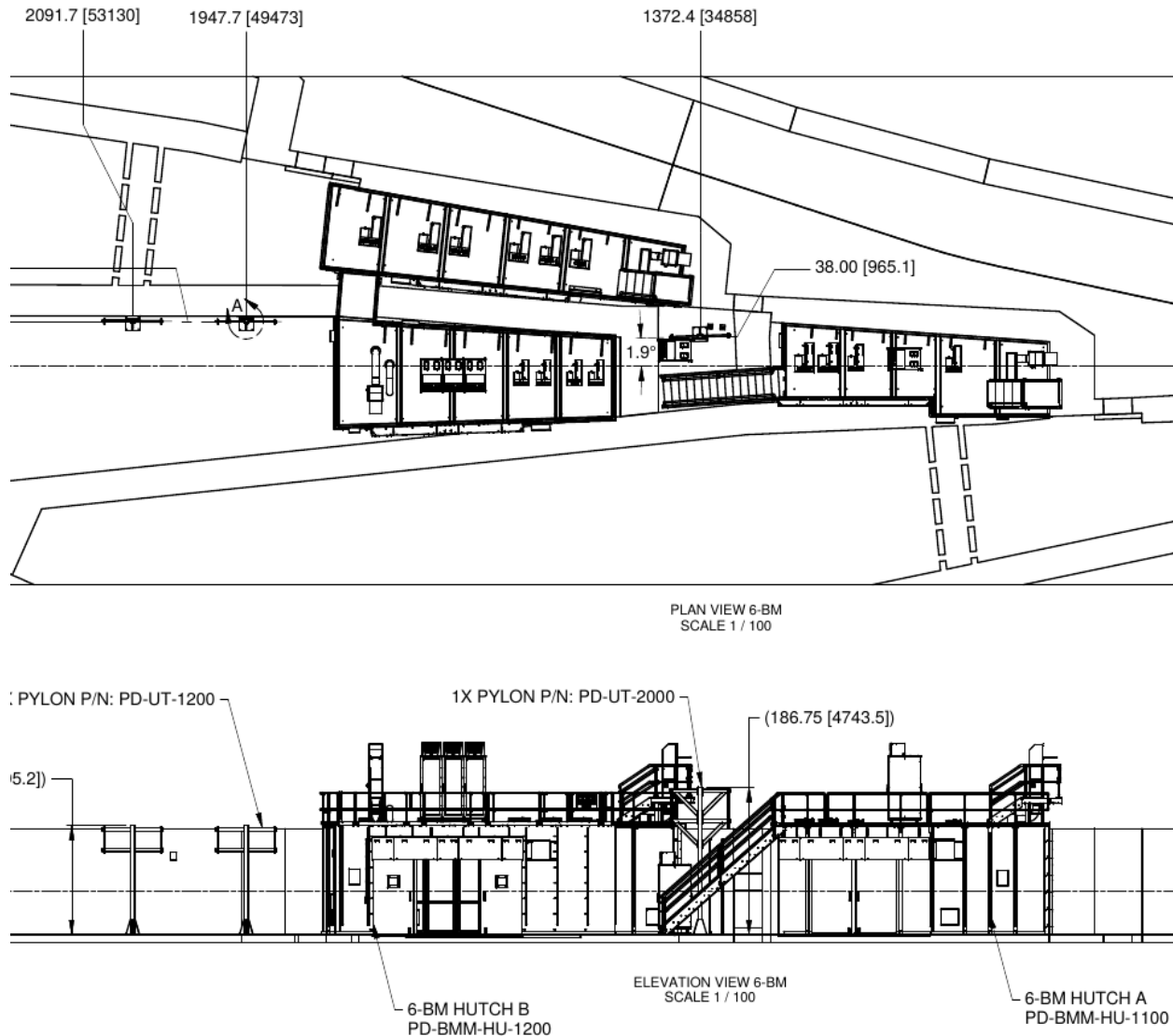


Figure 3.8: Pylon locations distributing utilities to the work area.

4 MAJOR TECHNICAL RISK ITEMS

The requirements on the optics are readily achievable today. No new technical advances are required for delivering the proposed capabilities. Much of the end station instrumentation was in use until the NSLS shutdown in September 2014. We anticipate the following technical risks:

4.1 Beamline complexity driven by mirror system operating modes

The variable positions of mirrors M2 and M3 lead to a variety of operating modes for the beamline. The height of the beam at the positions of the XAS and XRD end stations is different in each mode. This leads to a large configuration space, resulting in operational complexity of the beamline. This complexity can be managed by reliable, reproducible motion and encoding of mirrors M2 and M3 as well as the tables supporting the XAS station and the goniometer. As the beamline is commissioned, an exhaustive look-up table of motor positions will be constructed. Once a specific experiment is placed within one of the six operating modes, the control system can then drive all relevant motors to tabulated positions. The various beamline diagnostics, most importantly the NanoBPM and the fluorescent shield at the entrance to the end station, can be used to verify the beam position when entering an operating mode. With this exhaustive look-up table, it will be quick and easy to get to a sensible starting point for the setup of any experiment. Initial science commissioning will include time dedicated to experiments performed in each operating mode.

4.2 Relocation and re-use of end station equipment, poorly specified end station equipment

There is possibility of damage during equipment transfer of the end stations. Each item will be evaluated at the time of beamline commissioning, at the latest. Many things can be evaluated in advance of beamline commissioning.

The transferred end station equipment may not be compatible with NSLS-II standards in terms of safety, regulations, and software integration. This is a problem common at NSLS-II – many beamlines are repurposing equipment from NSLS beamlines. Addressing these issues will be relatively straightforward for us, given that we benefit by lessons learned by earlier beamlines.

At this time, a suitable table for the XAS end station has not been procured. In time, a table with five degrees of freedom (using the coordinates in the axis definitions at the beginning of this report, these degrees of freedom are X, Y, Θ_X , Θ_Y , and Θ_Z) sitting on a granite block for stability must be procured. In the short term, a table resting on a metal frame and providing Y and Θ_X is sufficient to commission the beamline. For initial commissioning, a four-axis table capable of motion in X, Y, and Θ_X has been borrowed from the dormant MID beamline effort.

4.3 Monochromator heat load

Finite Element Analysis is being performed for a few well-selected cases without filter (desirable), and with various filter combinations. The resulting slope errors will be compared with the rocking curve width of the first crystal at the simulated Bragg angle to evaluate the viability of the monochromator under each case. The risk can be further mitigated, at a cost of

reduced flux, by reducing the operating aperture or using more aggressive filtering.

4.4 Presence of M1 in the front end

Mirror M1 is situated in the front end. In the event of any problem related to vacuum conditions or misalignment of the optic, we may be required to wait until the next studies day to address the problem. This could result in loss of beamtime hours. To mitigate this risk, the vendor is mindful of the operational requirements of an inaccessible mirror and will strive to deliver a highly reliable instrument. For example, the drifting of motors resulting in a misalignment of this paraboloid optic would have a detrimental impact on the energy resolution of the beamline. To correct such a problem, we would require that the encoders return reliable position data. Following the lead of the vendors of the 23-ID undulators, we have specified 10 mm of lead shielding around the encoders, which are themselves chosen for their relative radiation-hardness. This shielding will prolong the life of these delicate but essential components.

4.5 Platinum substrate on mirrors M1 and M2

Mirrors M1 and M2 are coated with 50 Å Rh on 300 Å Pt. Given that the beamline is intended to measure XAS over an energy range that includes the Pt L edges, the energy response of the mirror in the energy range from 11500 eV to 14000 eV poses a risk for data quality.

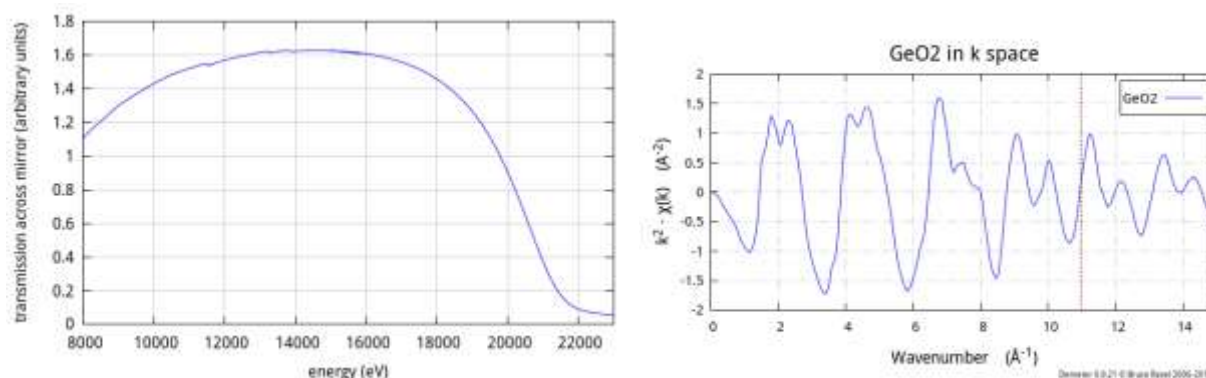


Figure 5.0:1: (Left) Response of a flat mirror with 50 Å Rh on 300 Å Pt. (Right) The k^2 -weighted $\chi(k)$ spectrum of a sample of GeO_2 measured in transmission after the flat mirror. The vertical line indicates the Pt L_3 edge energy at 11564 eV.

The left side of figure above shows the energy response of a flat mirror with the same coating as M1 and M2 measured at NSLS X23A2. The mirror angle was 3.5 mrad. On the right is the k^2 -weighted $\chi(k)$ spectrum of a powdered sample of GeO_2 measured in transmission after the mirror. Although the Pt L edges are discernable in the mirror response, there is no impact on the quality of the measured EXAFS data. The mitigation of this risk is the same as the mitigation of experimental risk in *any* EXAFS measurement – good sample preparation is a requirement for high quality data.

5 SAFETY

In addition to safety precautions related to the synchrotron source, the BMM beamline will provide proper emergency egress routes and a capacity to handle samples and make measurements in a safe manner.

Floor egress: The first optical enclosure and the experimental station are located in a relatively enclosed area, thus care must be taken to guarantee adequate egress routes in case of emergency. Two egress routes are provided; one standard walkway with unimpeded access from the FOE and end-station to the outboard walkway along the length of the beamline, and a duck-under path located downstream of the FOE with access to the SST egress routes. The egress routes are shown in green in the following figure. Note that the width of the path between the upstream end of the 6-BM-A hutch and the adjoining 6-ID floor space is very narrow. However, that stretch of hutch wall houses only the ventilation labyrinth and will never be occupied.

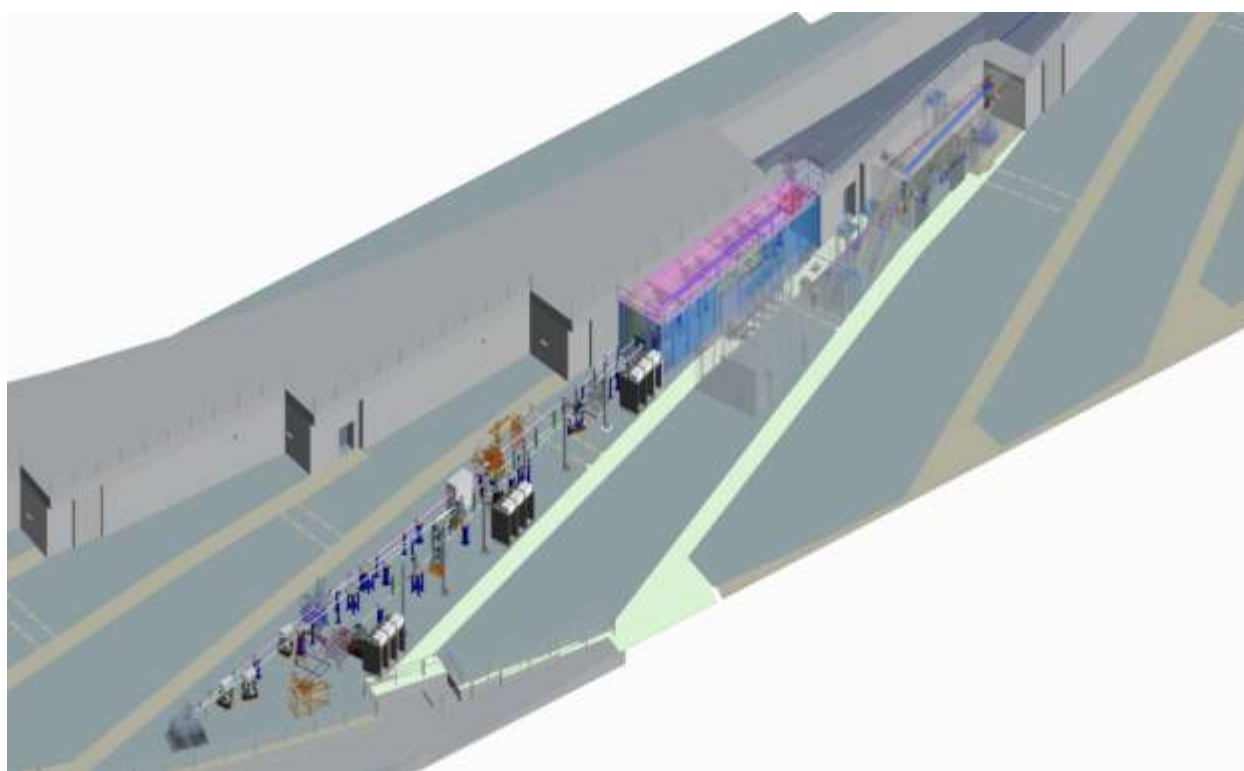


Figure 6.1: Egress routes from 6-BM

Roof egress: Egress from the roof of the end-station, which houses several electronics racks, is via the bridge to the 7-ID-A hutch, then to the storage ring tunnel roof. From there, the egress path continues counter-clockwise around the ring to the roof of the 6-BM-A hutch, then down the staircase to the floor, where the egress path connects with the routes described above. This path is shown in green in the following figure. An alternate egress route is through the interior doors on the mezzanine.

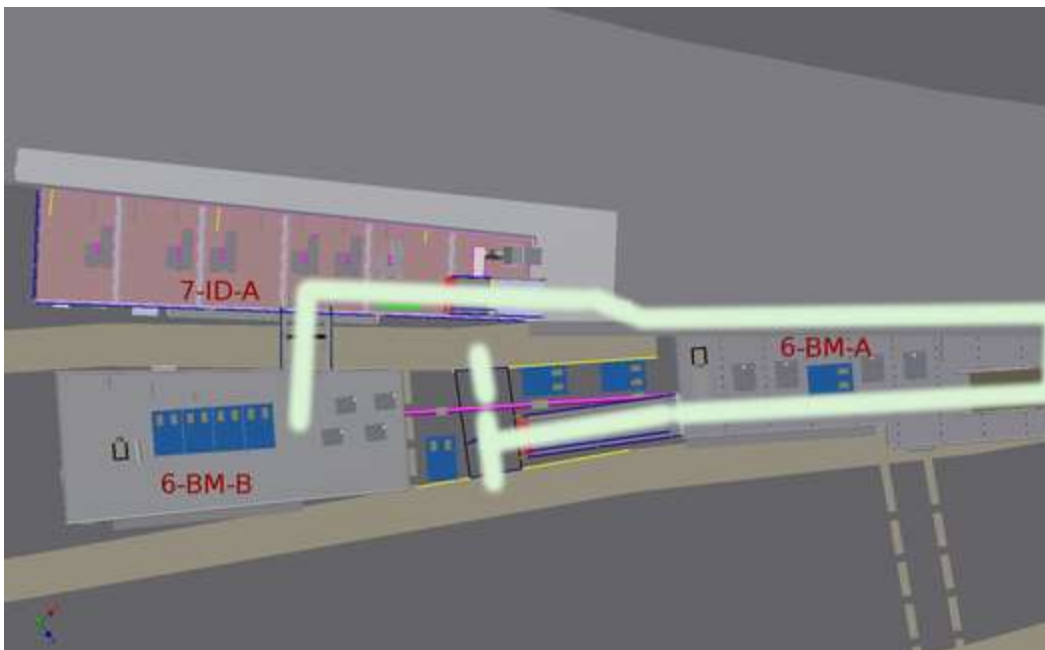


Figure 6.0:1: Egress from the roof of the end station. Note that bridge has since been repositioned to the end 6BM-B, but the egress pattern is unchanged.

Safe experimental practice: BMM is a general-purpose XAS and XRD beamline. The capability to handle a wide variety of samples with associated chemicals, gases, and environmental conditions is critical to the beamline mission. All experiments will follow standard safety approval protocol to verify required personnel protection equipment (PPE) for each given experiment and that approved protocol and work planning are done for every experiment. Hazardous waste will be either disposed of through the standard procedures at BNL or will be returned by the user to their home institution along with the samples. Proper training in the use of the beamline will be done by qualified beamline staff. Proper training will be required of all users for hazardous waste generation, cryogen safety, compressed gas handling, electrical safety, and so on as needed. Training related to proximity to the ISS hazardous gas handling facility may also be necessary.

Sample staging area: The large, open space downstream of the BMM end station will be used as common space for the NIST Spectroscopy Suite of beamlines. This will include control stations for BMM and some of the SST end-stations, storage, and sample preparation and staging space. The sample preparation space will be restricted to disposition of samples that do not require engineered controls or specific safety considerations. As an example, nanomaterials will be prepared elsewhere under appropriate conditions and be transported to the staging area with containment that is also appropriate for use in the hutch.

APPENDICES

Table A.1: Contents of supplemental documentation

Page numbers	Contents
1-5	BMM optical design report by Ruben Reininger (2011)
6	Design of M1 optical element
7	Design of M3 optical element

Focusing Options for the BMM Beamline at NSLS-II

Ruben Reininger
(Dated: February 23, 2011)

We describe three possible optical configurations of the BMM beamline collecting 1.5 horizontal mrad from a 3 pole wiggler (3PW) at NSLS-II. All system include a collimating mirror upstream the ratchet wall followed by a double crystal monochromator (DCM) and a refocusing mirror. Ray tracings through the full beamline show that the use of a toroid as the first element has a worse resolution than a paraboloid with reasonable figure error.

I. INTRODUCTION

As shown in Fig. 1 of our previous report [1], the vertical angular divergence of the three pole wiggler (3PW) radiation at 10 keV is larger than the reflection width of the Si(111) reflection. This means that the radiation needs to be vertically collimated prior to the crystal for preserving the intrinsic crystal resolution. Furthermore, we showed that there is an almost two fold increase in horizontal acceptance when the mirror (collimating in both directions) is placed upstream the ratchet wall.

The ideal optical element for collimating the 3PW radiation is a paraboloid, the second choice is a toroidal mirror. A 0.9 m long paraboloid or toroid located at 14 m from the source at an angle of incidence of 0.2 degrees (3.5 mrad) will collect 1.5 mrad horizontally and most of the radiation emitted by the 3PW in the vertical direction at 10 keV. The first mirror length is only 0.9 m since the mirror focusing this radiation after the monochromator needs to be almost 1.2 m long.

II. OPTICAL SYSTEMS

We contacted several mirror manufacturing companies asking for the feasibility of making the required mirrors and their expected slope errors within a budget of \$80,000-120,000 per mirror. Their replies were as follows:

1. One manufacturer quoted 5 μ rad RMS meridional and 40 μ rad RMS sagittal for one paraboloid or below 2 μ rad RMS meridional for two identical mirrors. For the toroid they quoted 0.5 μ rad RMS meridional and 10 μ rad sagittal.

2. Second vendor quoted 5 μ rad RMS meridional slope error for the paraboloid and smaller slope error at a higher price.

3. Third vendor quoted 2.5 μ rad RMS meridional and 25 μ rad RMS sagittal for the paraboloid for \approx \$160,000 with support and cooling provision and \$80,000 for a

toroid with 1.5 μ rad RMS meridional and 15 μ rad sagittal.

4. We did not receive a reply from the fourth vendor.

We compared the energy resolution and intensity distribution at the focal plane of the BMM beamline at NSLS-II assuming three different optical configurations:

1. PP: A paraboloid mirror (focal length=14 m) collimating the beam in both directions and a paraboloid focusing the collimated light.

2. PT: A paraboloid mirror (focal length=14 m) collimating the beam in both directions and a toroid ($R=9.5$ km, $\rho=97.7$ mm) focusing the collimated light.

3. TT: A toroidal mirror “collimating” the beam in both directions and a toroid focusing the collimated light. Both with $R=8.02$ km, $\rho=97.7$ mm.

III. RESULTS

The ray tracings described below were performed using the SHADOW code [2]. The electron RMS source size at the position of the 3PW is $167 \times 12.3 \mu\text{m}^2$ (hor. \times ver.) [3]. For energies between 10 and 30 keV and for an horizontal collection angle of 1.5 mrad, the 3PW source can be approximated (within $\approx 15\%$ error in flux) as a bending magnet with a 1.14 T field. The two other magnets of the 3PW are much weaker and have a much smaller flux contribution at these energies. A 200000 points “synchrotron” type source with a “continuous energy distribution”, centered at 10 keV or 20 keV, was used in the ray tracings.

The first mirror is located inside the ratchet wall at a distance of 14 m from the three pole wiggler (3PW). The double crystal monochromator (DCM) equipped with Si(111) and Si(311) crystals is located 14 m downstream the collimating mirror followed by the refocusing mirror 4 m downstream the DCM. The final focus is 14 m downstream the refocusing mirror. We note in passing that the calculated meridional radius for the collimating and focusing toroids is 8.02 km. However, a slightly better

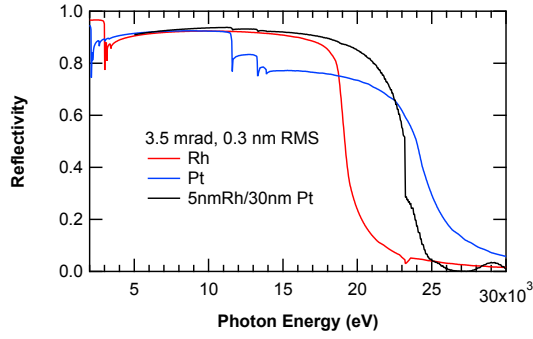


FIG. 1. Reflectivity of Rh, Pt, and of a double layer consisting of 5 nm Rh over 30 nm Pt. The angle of incidence is 0.2 degrees and we assumed an RMS roughness of 0.3 nm

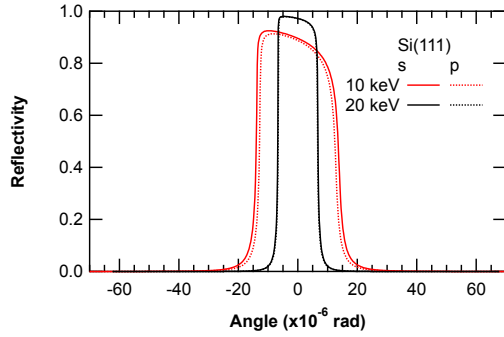


FIG. 2. Rocking curve of Si(111) for s and p polarization at 10 and 20 keV.

focus is achieved in the PT system when the meridional radius is 9.5 km.

Rh was used as the optical coating on both mirrors in the ray tracings. Fig. 1 compares the reflectivity of Rh to that of platinum at a grazing angle of 3.5 mrad including a RMS roughness of 0.3 nm (SRCalc code [4] using the optical constants in [5]). As seen in the figure it is advantageous to use Rh instead of Pt up to 19 keV at this angle of incidence. The third trace in the figure is discussed below.

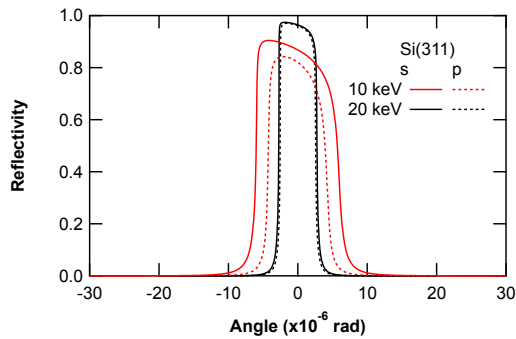


FIG. 3. Rocking curve of Si(311) for s and p polarization at 10 and 20 keV.

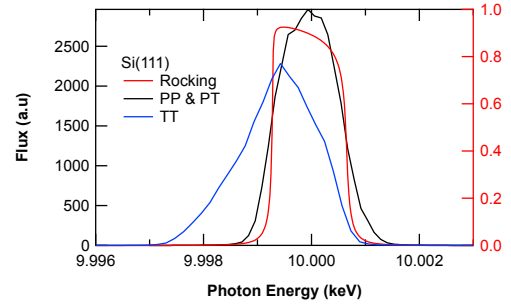


FIG. 4. Left axis: Flux as a function of the photon energy. Black: PP and PT; Blue: TT. Right axis and red trace: Reflectivity of double crystal monochromator in collimated light. Si(111) crystals.

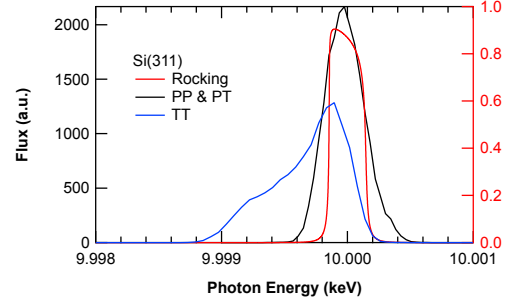


FIG. 5. As Fig. 4 with Si(311) crystals.

The BRAGG routine in SHADOW was used to generate the Si(111) (Fig. 2) and Si(311) (Fig. 3) reflection curves. Meridional (sagittal) RMS slope errors of 2.5 (25) μ rad in the paraboloids and 1.0 (10) μ rad in the toroids were assumed in the ray tracings.

The output from SHADOW including the photon energy and amplitude (containing the Rh and Si reflectivities) of each ray was used to create the histograms giving the energy resolution (Figs. 4-7) and the 3D plots (Figs. 9-11) showing the beam profile at the sample position.

As seen in Figs. 4-7 the resolution of all systems is worst than that of the corresponding double crystals in

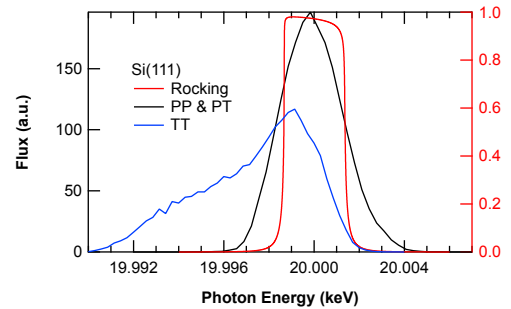


FIG. 6. As Fig. 4 at around 20 keV

TABLE I. Total flux when using the Si(111) crystal and Si(311) for the optical arrangements at photon energies of 10 and 20 keV. The SD sizes vary only slightly with polarization and photon energy.

	PP	PT	TT
10 keV (111) (10^{12} Phot./s)	2.0	2.0	1.9
10 keV (311) (10^{11} Phot./s)	4.1	4.1	3.8
20 keV (111) (10^{10} Phot./s)	5.9	5.9	5.4
20 keV (311) (10^{10} Phot./s)	1.2	1.2	1.1
Size (hor \times ver.) (mm \times mm)	0.17 \times 0.11	0.18 \times 0.18	0.2 \times 0.06

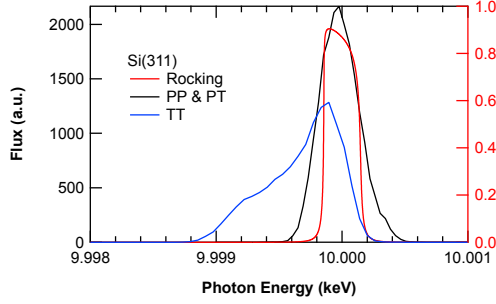


FIG. 7. As Fig. 6 with Si(311) crystals.

collimated light and significantly worst for the TT system. We note that the energy resolution of the PP and PT systems is the same since they have the same first three optical elements. The degradation in energy resolution in the PP (and PT) systems is due to the meridional slope errors we have assumed. Better optics will improve the energy resolution. The resolution degradation in the TT system is asymmetric towards the low energy and it is due to the large aberration of the toroid. This aberration can be easily seen (Fig. 8) in the histogram of the vertical divergence of the beam after the reflection by the

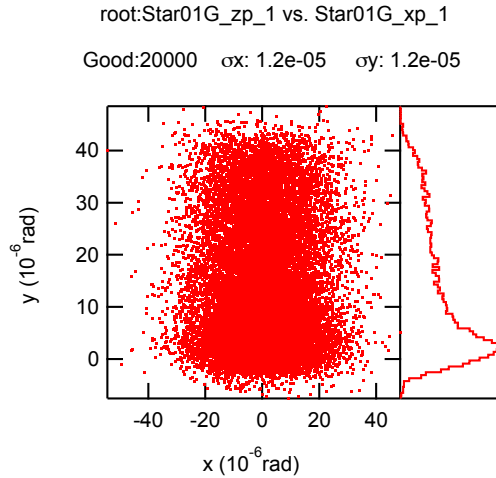


FIG. 8. Scatter plot of the divergence after the first toroidal mirror in the TT system. x is horizontal and y is vertical

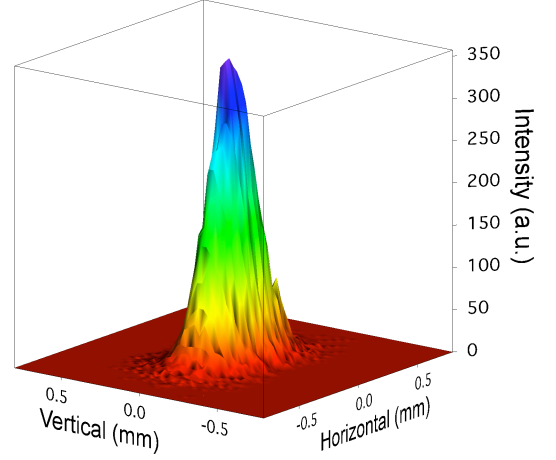


FIG. 9. Intensity at the focal plane when using two paraboloids and Si(111) crystals at 10 keV.

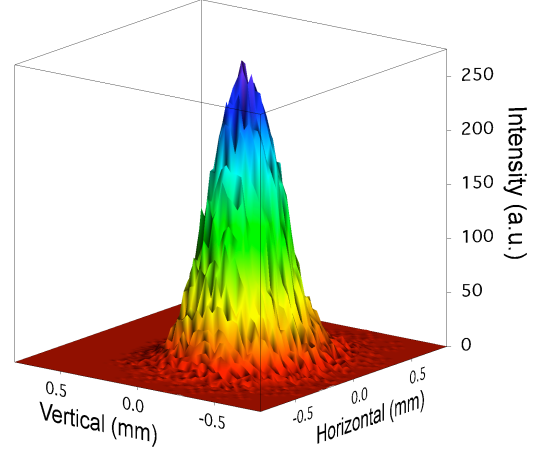


FIG. 10. Intensity at the focal plane when using a paraboloid followed by a toroid and Si(111) crystals at 10 keV.

first toroid. The resolution in the TT system can be improved by reducing the horizontal acceptance of the first toroid. Collecting 0.75 mrad horizontally instead of 1.5 improves the resolution of the TT system to approximately that of the PP (and PT) systems.

Table I summarizes the expected flux at the sample for the three focusing options when using either the Si(111) or Si(311) crystals. The flux at a given energy and for a set of crystals is the same for either the PP or PT configuration and slightly less for the TT configuration due to geometrical losses at the second toroid in the TT system. Approximately 94% of the flux is horizontally polarized. Using Si(311) crystals instead of Si(111) reduces the flux by almost a factor of five whereas the improvement in resolution (based on the standard deviation (SD) of the resolution obtained from Figs. 4-7) is less than a factor of three. Since both the mirrors and crystals reflectivity varies only slightly between 10 keV and 18 keV, the flux

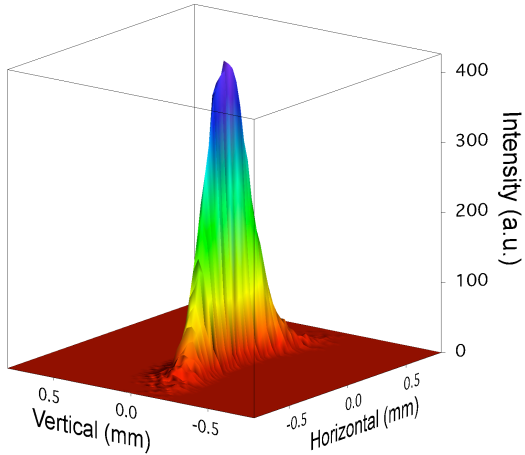


FIG. 11. Intensity at the focal plane when using two toroids and Si(111) crystals at 10 keV.

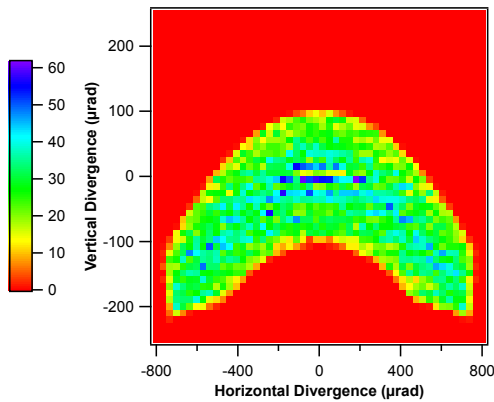


FIG. 12. Image plot of the beam divergences downstream the second toroid in the TT system using the Si(111) at 10 keV.

in this energy range can be easily scaled based on the flux emitted by the insertion device. The scaling factors relative to 10 keV are 0.56 for 15 keV and 0.38 at 18 keV.

The standard deviation of the beam size along the horizontal and vertical directions at the focal plane are also listed in table I. The horizontal SD in the three systems is close to the expected 1:1 magnification. The sizes along the vertical direction are mostly determined by the slope errors on the mirrors and the imaging aberrations of the toroids.

Figs. 9-11 show the 3D plots of the intensity as a function of the transverse coordinates at the focal plane. Both the PP and TT systems clearly show the much wider beam along the horizontal direction. The aberrations of the PT system increase the vertical size to the same value of the horizontal.

The beam divergence at the focus position is very sim-

ilar in all cases. A typical image plot downstream the second toroidal in the TT system is shown in Fig. 12. The root mean square (RMS) values of the horizontal and vertical divergences in this case are 0.4 mrad and 0.1 mrad, respectively.

The above results show that the PP and PT configuration are very similar. The PP configuration has two drawbacks besides costs: A paraboloid is more complicated to align and the BMM beamline requires a variable spot size at the sample which cannot be achieved with a fixed paraboloid.

The advantage of the PT configuration is the fact that instead of a fixed toroid one could implement a sagittal cylinder that can be bent to a toroid with the correct meridional radius. The mirror could be used without bending to reduce the divergence along the vertical direction and also to focus the beam along the vertical direction at second experimental station.

Replacing the toroidal mirror in the PT system by a sagittal cylinder with the same sagittal radius as the toroid yields a spot with the same horizontal size and divergence but a spot with a 0.8 mm RMS vertical size and a vertical RMS divergence of 35 μ rad. By limiting the horizontal acceptance to 0.75 mrad decreases the vertical divergence to 10 μ rad RMS.

One point worth mentioning and investigating concerns the results presented in Fig. 1. We have also plotted in the figure the reflectivity of a double layer coating, i.e., 5 nm of Rh over 30 nm of platinum. As seen in the figure, the Pt edges are not seen in the reflectivity curve of the double layer and in addition, there is a significant enhancement in the reflectivity between 20 and 23 keV. The main concern would be an interlayer diffusion that could impair the calculated reflectivity. I strongly recommend to investigate the performance of the double layer coating.

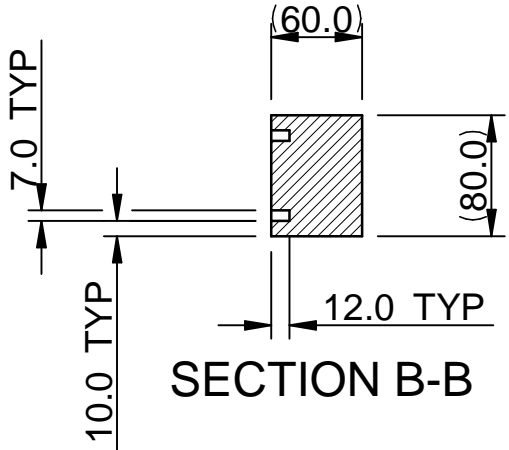
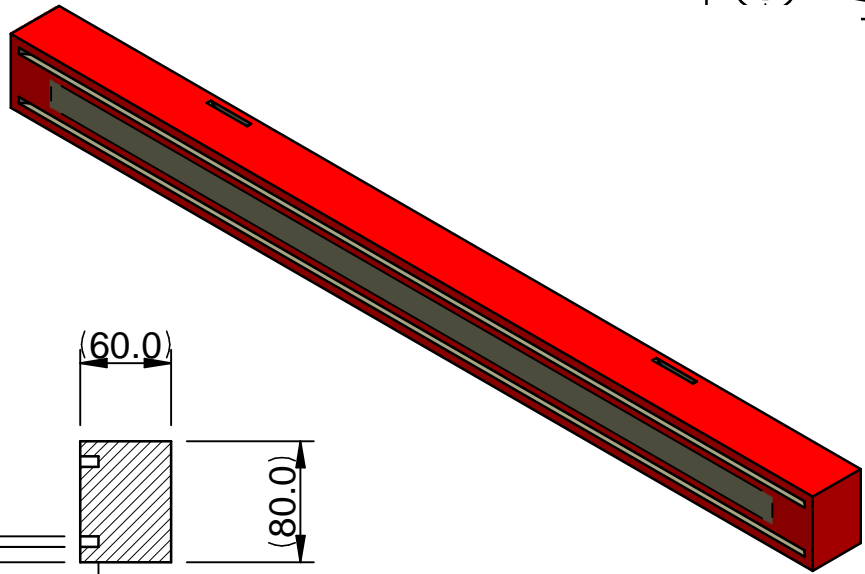
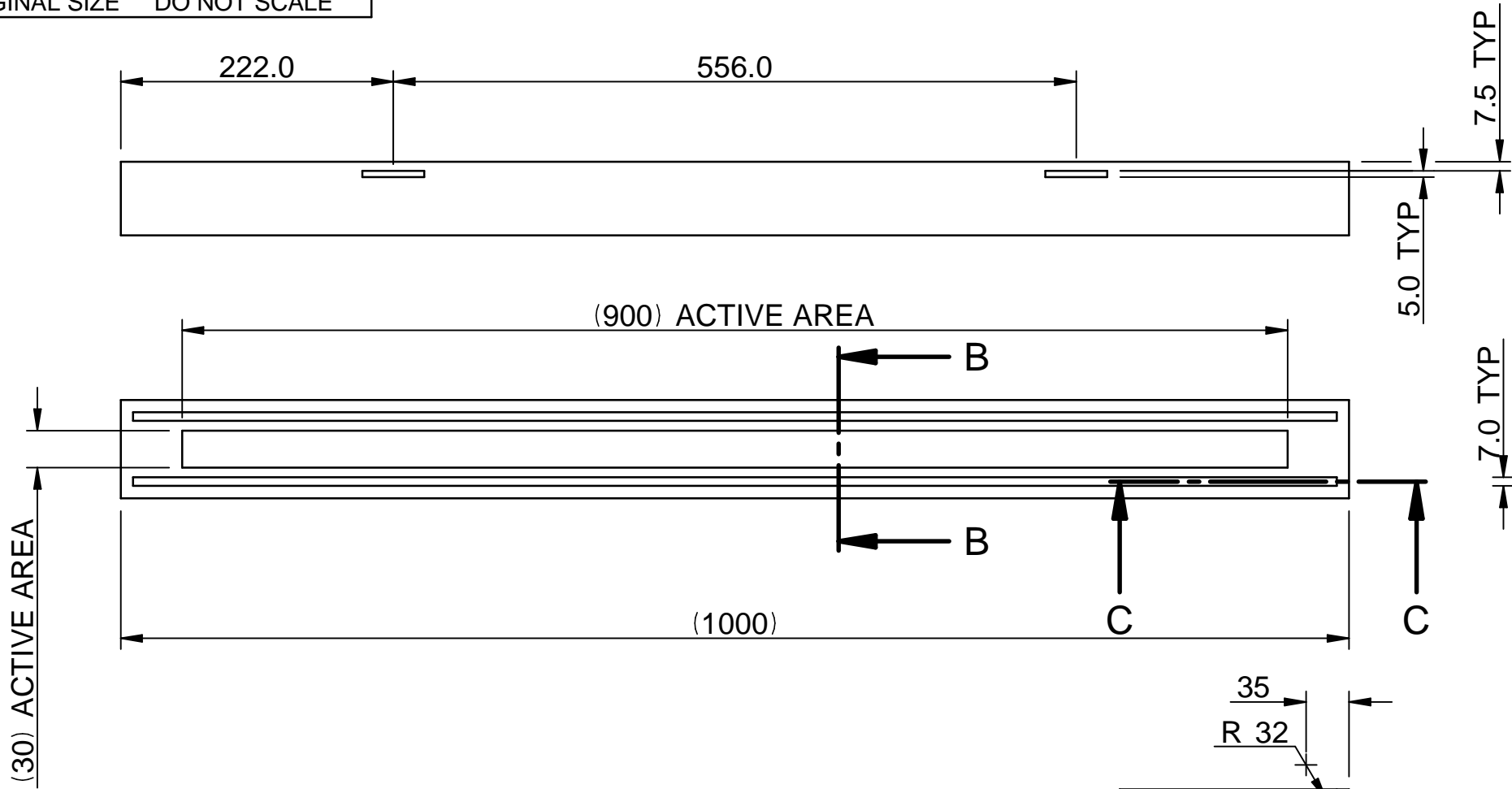
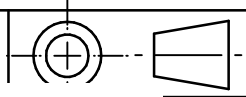
IV. COOLING REQUIREMENTS

The total power incident on the first optical element with 0.5A stored in the 3 GeV storage ring is 63 W. The first mirror absorbs slightly less than 10 W and the absorbed power density is almost 0.1 mW/mm². Both the absorbed power and power densities are very low, nevertheless, cooling should be provided to remove the resulting heat.

The power incident on the first crystal monochromator is almost 53 W. Most of this power will be absorbed by the first crystal of the monochromator and should be efficiently removed.

The power incident on the second mirror is negligible (less than 10 mW) and therefore this mirror does not require any cooling.

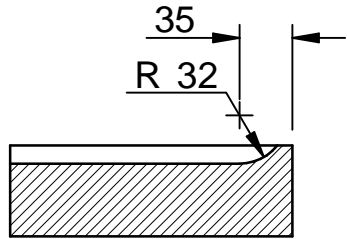
-
- [1] R. Reininger, *Focusing the 3PW radiation at NSLS II*, Tech. Rep. (REPORT, 2010). 041410/03%20Shen.ppt.
- [2] C. Welnak, G. Chen, and F. Cerrina, Nucl. Instr. and Meth. A **347**, 344 (1994).
- [3] Q. Shen(2010), <http://www.bnl.gov/nsls2/docs/ppt/>
- [4] R. Reininger, "Srcalc," (2001-2011).
- [5] B. Henke, E. Gullikson, and J. Davis, Atomic Data and Nuclear Tables **54**, 181 (1993).



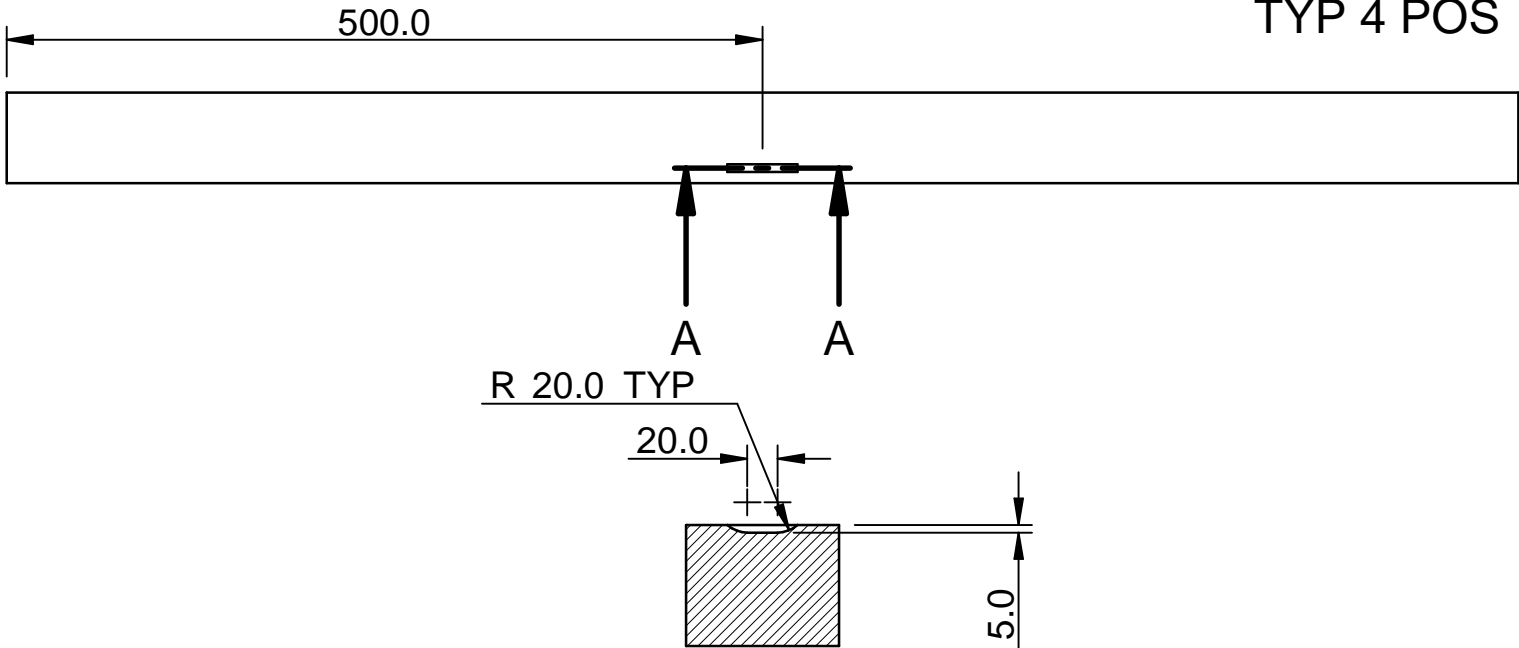
SECTION B-B

- NOTES:-
- 1. THIS IS A UHV COMPONENT
 - 2. NO SILICONE OR SULPHUR BASED FLUIDS ARE TO BE USED
 - 3. REMOVE ALL BURRS & SHARP EDGES

Substrate material	Single crystal silicon <100>
Substrate dimensions	1000 mm L x 80 mm W x 60 mm D
Active Area (centred on substrate to within ± 0.5mm)	900 mm x 30 mm
Grazing incidence angle, P, Q	3.5 mrad (0.2°), 13m, ∞
Substrate Shape	Paraboloid
Tangential slope error	< 2.5 μrad RMS over active length in frequency range L ⁻¹ to 1 mm ⁻¹
Sagittal slope error	<25 μrad RMS over active length on prepared substrate in frequency range W ⁻¹ to 1 mm ⁻¹
Coating	Rh 5 nm ± 10% thick on Pt 30 nm
Surface Roughness	<0.3 nm RMS in frequency range 0.005 to 1 μm ⁻¹ . No points over 0.8 nm permitted.
Surface Quality	0.5 scratches (>2mm x 5 μm) or points (>50 μm diameter) per cm ² over active optical area
Cooling	Slot Cooled



SECTION C-C
TYP 4 POS



SECTION A-A
TYP 3 POS

REV	DATE	DMR	DESCRIPTION
-	-	-	-
-	-	-	-
-	-	-	-
-	-	-	-

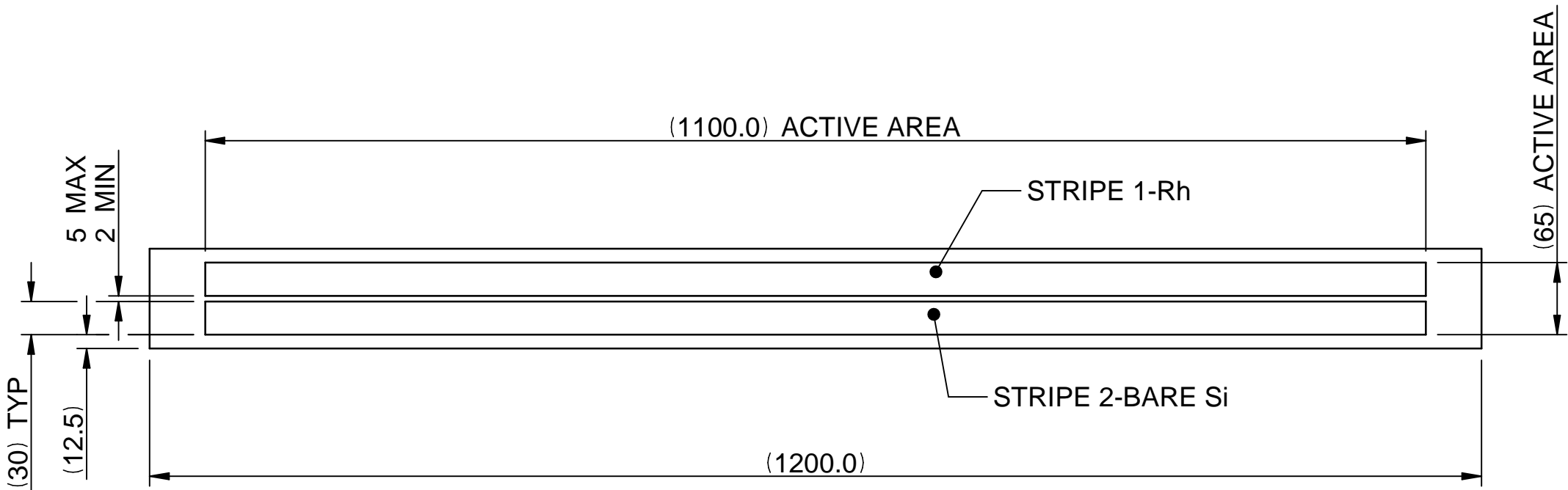
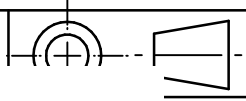
TOLERANCES UNLESS STATED	
X	± 0.5mm
X.X	± 0.3mm
X.XX	± 0.1mm
ANGLE	± 0°15'

MATERIAL: SEE NOTES	
SURFACE FINISH 1.6μm	FINISH: CLEAN
UNLESS STATED	SHEET 1 OF 1
mm	DATE
UNLESS STATED	16/02/15

DESCRIPTION	
M1 (V+HCM) OPTIC-BMM-NIST	
DRAWN	STATUS
julian.wiatrzyk	Work


DRAWING NUMBER		REV
AMC1588		01





- NOTES:-
- 1. THIS IS A UHV COMPONENT
 - 2. NO SILICONE OR SULPHUR BASED FLUIDS ARE TO BE USED
 - 3. REMOVE ALL BURRS & SHARP EDGES

Operating position	Vertically deflecting downwards
Substrate material	Single Crystal Silicon
Active area	1100 mm x 65 mm
Blank dimensions	1200mmL x 90mmW x 60mmD
Shape	Plane, R>40km
Incidence Angle, P, Q	3.5 or 5 mrad, ∞, ∞
Tangential slope error	<0.5 μrad RMS over active length in frequency range L ⁻¹ to 1mm ⁻¹ with >40 km radius removed at ~4.8 mm resolution
Sagittal slope error	<10 μrad RMS in frequency range W ⁻¹ to 1mm ⁻¹ with >40 km radius removed
Stripes	Stripe 1, Rh 5 nm on Pt 30 nm, 30mm wide on 10 nm Cr binder layer Stripe 2, Bare Si, 30mm wide
Coating Density	>95% of bulk material
Surface Roughness	<0.3 nm RMS in frequency range 0.005 to 1μm ⁻¹ . No points over 0.8 nm permitted
Surface Quality	<0.5 scratches (>2mm x 5μm) or points (>50μm diameter) per cm ² over active optical area
Cooling	Uncooled

	-	-	-		TOLERANCES UNLESS STATED		MATERIAL: SEE NOTES			DESCRIPTION M3 (HRM) OPTIC-BMM-NIST					
	-	-	-		X ± 0.5mm		SURFACE FINISH 1.6µm								
	-	-	-		X.X ± 0.3mm		FINISH: CLEAN								
	-	-	-		X.XX ± 0.1mm										
					ANGLE ± 0°15'		UNLESS STATED			SHEET 1 OF 1			mm		
REV	DATE	DMR	DESCRIPTION				DATE			DRAWN		STATUS		DRAWING NUMBER	REV
							16/02/15			julian.wiatrzyk		Work		AMC1692	01
THIS DRAWING BELONGS TO FMB OXFORD. THIS DRAWING HAS BEEN ISSUED ON CONDITION THAT IT IS NOT COPIED, REPRINTED OR DISCLOSED EITHER WHOLLY OR IN PART DETAIL TO A THIRD PARTY WITHOUT PRIOR CONSENT IN WRITING FROM FMB OXFORD, OSNEY MEAD, OXFORD, ENGLAND ©2015															